On the extension of the Gurson-type porous plasticity models for prediction of ductile fracture under shear-dominated conditions

Jun Zhou [a], Xiaosheng Gao [a,*], James C. Sobotka [b], Bryan A. Webler [b], Brian V. Cockeram [b]

[a] Department of Mechanical Engineering, University of Akron, Akron, OH, USA
[b] Bechtel Marine Propulsion Corporation, West Mifflin, PA, USA

ABSTRACT

One of the major drawbacks of the Gurson-type of porous plasticity models is the inability of these models to predict material failure under low stress triaxiality, shear dominated conditions. This study addresses this issue by combining the damage mechanics concept with the porous plasticity model that accounts for void nucleation, growth and coalescence. In particular, the widely adopted Gurson–Tvergaard–Needleman (GTN) model is extended by coupling two damage parameters, representing the volumetric damage (void volume fraction) and the shear damage, respectively, into the yield function and flow potential. The effectiveness of the new model is illustrated through a series of numerical tests comparing its performance with existing models. The current model not only is capable of predicting damage and fracture under low (even negative) triaxiality conditions but also suppresses spurious damage that has been shown to develop in earlier modifications of the GTN model for moderate to high triaxiality regimes. Finally the modified GTN model is applied to predict the ductile fracture behavior of a beta-treated Zircaloy-4 by coupling the proposed damage modeling framework with a recently developed J_2–J_3 plasticity model for the matrix material. Model parameters are calibrated using experimental data, and the calibrated model predicts failure initiation and propagation in various specimens experiencing a wide range of triaxiality and Lode parameter combinations.

© 2014 Elsevier Ltd. All rights reserved.

1. Introduction

Microvoid nucleation, growth and coalescence, has been regarded as a common mechanism of ductile failure of metals and alloys. Early studies by McClintock (1968) and Rice and Tracey (1969) on growth of cylindrical and spherical voids in infinitely large, plastic solids showed the major parameters in this fracture process and suggested possible further developments towards mechanism-based, micromechanical models that describe the complex ductile failure process. Later Gurson (1977) proposed a homogenized yield surface for void-containing materials based on the maximum plastic work principle, and Rousselier (1987) described the mechanical behavior of voided materials using thermodynamic and plastic potentials. More recent efforts on this area have focused on extending/modifying these models to develop computational schemes that simulate the ductile fracture process under various circumstances. Tvergaard (1981, 1982) introduced two adjustment parameters into the Gurson model to account for the effect of void interaction and material strain hardening. Chu

and Needleman (1980) proposed void nucleation models controlled by the local stress or plastic strain. Tvergaard and Needleman (1984) introduced a simplified method to provide for rapid deterioration of stiffness after localization has occurred in the material. Koplik and Needleman (1988) proposed a unit cell approach to calibrate the micromechanical parameters of the homogenized model. Gologanu et al. (1993, 1994) extended the Gurson model and derived a yield function for materials containing spheroidal voids. The Gurson model, with additional developments by Tvergaard and Needleman, is often referred as the GTN model. For the Gurson-type model, the prediction of ductile fracture comes out naturally through the progressive loss of load carrying capacity at the material level. With the existence of a critical porosity to predict ductile fracture, the porosity serves not only as an internal variable, but also as a "failure indicator". To address the mesh sensitivity issue inherited from the lack of a length scale in the material model, Xia et al. (1995) and Gao et al. (1998) presented a computational cell approach based on the GTN model and predicted the constraint effect on ductile fracture. This idea of representing material in the fracture process zone as cell elements governed by the GTN model has been widely employed by the computational fracture mechanics community in recent years.

* Corresponding author. Tel.: +1 330 972 2415; fax: +1 330 972 6027.
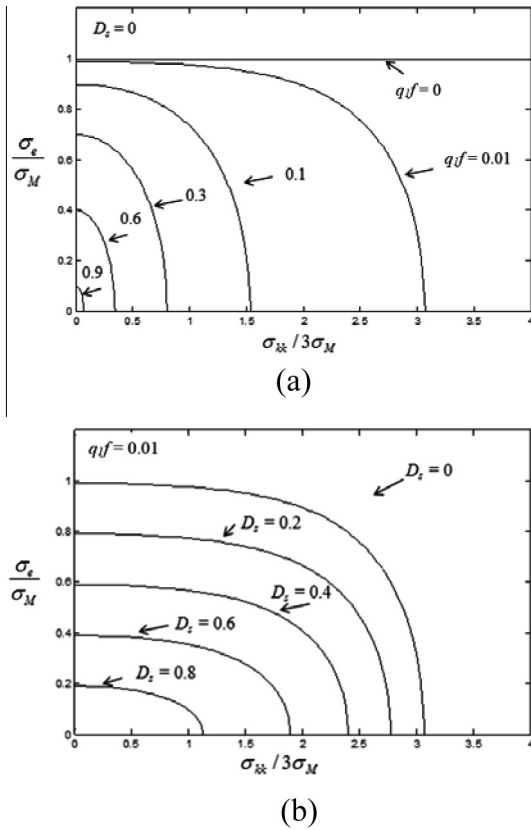 E-mail address: xgao@uakron.edu (X. Gao).

Fig. 1. Effect of volumetric damage and shear damage on the yield surface: (a) $D_s = 0$, (b) $q_1 f = 0.01$.

Despite the apparent success and wide popularity of the GTN model in predicting ductile fracture, it still suffers from several limitations (Benzerga and Leblond, 2010). A major drawback of the GTN model is its inapplicability to model localization and ductile fracture under low stress triaxiality, shear dominated deformations, since it does not predict void growth and damage under shear loading. Recent modifications have been motivated by this limitation to include shear-induced damage in the GTN model, among which the work by Xue (2008) and Nahshon and Hutchinson (2008) have received the most attention. These modifications preserve the original form of the GTN model while treating the void volume fraction in the model as a generalized damage parameter driven by a volumetric contribution that represents the traditional void nucleation, growth and coalescence processes *and* a deviatoric contribution that incorporates void shearing mechanisms. These modifications show improvement in predicting ductile damage under low triaxiality conditions but indicate excessive and spurious damage in the cases of moderate to high triaxiality. Nielsen and Tvergaard (2010) recognized this problem and introduced an ad hoc modification to the shear damage evolution law to reduce shear damage under high triaxiality. Moreover, these modified GTN models are shown to over-predict the volume change and thus result in unreasonable numerical results under shear-dominated conditions.

To resolve the problems faced by the existing models, a new extended GTN model is proposed in this study by combining the damage mechanics concept of Lemaitre (Lemaitre, 1985; Lemaitre and Lippmann 1996) with the GTN void growth model. Lemaitre's continuum damage mechanics (CDM) model treats the effect of damage in a purely phenomenological way and does not explicitly describe the details in the microstructure. It is based on the idea that the actual sustainable stress level in the material increases

Table 1
Model parameters for extended GTN model used in the single material point analyses.

q_1	q_2	f_0	f_c	f_f	ε_f^s	n	k
1.5	1	0.005	0.1	0.25	1.4	5	0.7

due to the reduction of the effective load bearing area resulted from defects such as micro-cracks or micro-voids. In this framework, a damage variable is introduced as the internal variable to the plasticity model without the details of the micro features being defined. Similar to using the porosity in a GTN model as a "failure indicator", the damage variable in CDM is also used as a "failure indicator". The CDM model is widely used in literature with various damage definitions, e.g., Chaboche (1988) and Xue (2007). By combining the GTN model with the CDM concept, two damage parameters, the volumetric damage (effective void volume fraction) and the shear damage, are coupled into the yield function and flow potential. The evolution law for void volume fraction remains the same as in the original GTN model and a new shear damage evolution law is proposed. Separate critical damage condition is used for volumetric damage and shear damage and complete material failure is said to have occurred if the total damage parameter (a combination of volumetric damage and shear damage) reaches unity. By doing this, the proposed model can no longer be regarded as a micromechanical model but a phenomenological one.

This paper is organized as follows. In Section 2 we first briefly review the GTN model and the recent modifications by Xue (2008) and Nahshon and Hutchinson (2008). A new model is presented after the discussions of the drawbacks of the existing models. The effectiveness of the new model is illustrated through a series of numerical tests that compare its performance with existing models in the literature. In Section 3 we apply the new model to predict the ductile fracture behavior of a beta-treated Zircaloy-4, where the elastic–plastic response of the undamaged material exhibits tension–compression asymmetry and is described by a recently developed J_2–J_3 model (Zhai et al., 2014). The material constants involved in the model are determined based on the experimental observations reported by Cockeram and Chan (2009, 2012) as well as model calibrations using experimental data reported in Zhai et al. (2014). The predicted failure initiation and propagation behavior and load–displacement response of specimens experiencing a wide range of stress states are compared with experiments. Finally some concluding remarks are made in Section 4.

2. The ductile failure model

In this section, we first briefly describe the GTN model as well as recent modifications by Xue (2008) and Nahshon and Hutchinson (2008). After discussing the drawbacks of these existing models, we present a new, modified model by combining the damage mechanics concept and the void growth model.

2.1. The original GTN model

To date, the most widely used micromechanical model for ductile fracture descends from Gurson with extensions by Tvergaard and Needleman (Gurson, 1977; Tvergaard, 1981, 1982; Tvergaard and Needleman, 1984). The yield function of the GTN model takes the following form

$$\Phi = \left(\frac{\sigma_e}{\sigma_M}\right)^2 + 2q_1 f \cosh\left(\frac{q_2}{2}\frac{\sigma_{kk}}{\sigma_M}\right) - 1 - (q_1 f)^2 = 0, \tag{1}$$

where: f is the current void volume fraction; σ_e is the macroscopic effective stress; σ_{kk} is the hydrostatic stress; and σ_M is the current
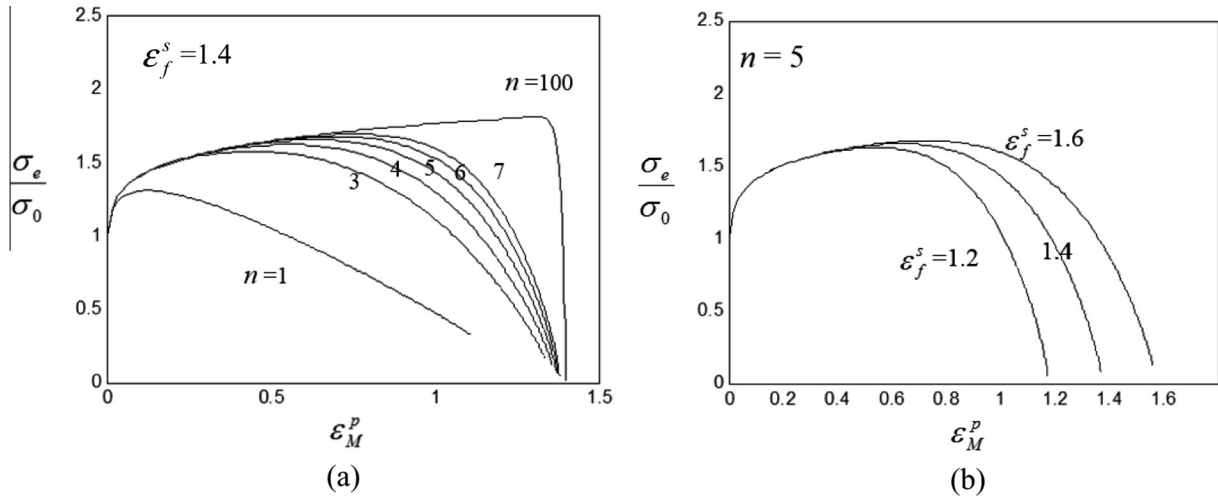
Fig. 2. Effects of n and ε_f^s on the effective stress vs. matrix plastic strain response under pure shear loading.

yield stress of the matrix material. The adjustment parameters q_1 and q_2 were introduced by Tvergaard (1981, 1982) to improve model predictions.

The plastic strain rate is defined as

$$\dot{\varepsilon}_{ij}^p = \dot{\lambda} n_{ij}, \tag{2}$$

where $\dot{\lambda}$ is the plastic multiplier and the associated (normality) flow rule is invoked to define the normal of the plastic strain rate, i.e., $n_{ij} = \frac{\partial \Phi}{\partial \sigma_{ij}}$.

The evolution of the void volume fraction is due to two contributions, void growth and void nucleation.

$$\dot{f} = \dot{f}_g + \dot{f}_n. \tag{3}$$

Void growth is based on bulk material incompressibility under plastic deformation

$$\dot{f}_g = (1 - f)\dot{\varepsilon}_{kk}^p, \tag{4}$$

where $\dot{\varepsilon}_{kk}^p$ represents the first invariant of the plastic strain rate.

Void nucleation can be stress or strain controlled. A commonly used strain-controlled void nucleation law is taken to follow a normal distribution as suggested by Chu and Needleman (1980)

$$\dot{f}_n = A_N \dot{\varepsilon}_M^p, \quad A_N = \frac{f_n}{S_n \sqrt{2\pi}} \exp\left[-\frac{1}{2}\left(\frac{\varepsilon_M^p - \varepsilon_n}{S_n}\right)^2\right], \tag{5}$$

where ε_M^p represents the matrix plastic strain, and f_n, ε_n and S_n are material parameters.

In the GTN model, the effect of void coalescence is taken into account by replacing f in Eq. (1) with an effective porosity f^* defined by the following bilinear function

$$f^* = \begin{cases} f & \text{for} \quad f \leqslant f_c \\ f_c + \frac{1/q_1 - f_c}{f_f - f_c}(f - f_c) & \text{for} \quad f_c \leqslant f \leqslant f_f \end{cases}, \tag{6}$$

where f_c is the critical void volume fraction at which void coalescence begins and the material softening is accelerated thereafter. Another material constant is the void volume fraction cutoff at failure f_f. As f reaches f_f, f^* increases to $1/q_1$ and the material loses all stress carrying capacity.

By enforcing equality between the rates of macroscopic plastic work and the matrix plastic dissipation, the matrix yield stress, σ_M, and the matrix plastic strain rate, $\dot{\varepsilon}_M^p$, are coupled through

$$\sigma_{ij}\dot{\varepsilon}_{ij}^p = (1 - f)\sigma_M \dot{\varepsilon}_M^p \tag{7}$$

where the matrix material follows a prescribed hardening function $\sigma_M(\varepsilon_M^p)$.

2.2. Modified GTN models by Xue (2008) and Nahshon and Hutchinson (2008)

Eq. (4) indicates shear deformation does not trigger void growth and consequently, the original GTN model does not predict failure under shear deformation. Because of this limitation, Gao and Shih (1998) had to introduce ad hoc strain controlled void nucleation when they tried to use the GTN model to study mixed mode I/III ductile fracture. Recently Xue (2008) and Nahshon and Hutchinson (2008) proposed similar modifications to the original GTN model to incorporate the shear induced damage. In these modifications, the void volume fraction that appears in Eq. (1) is replaced by a general damage parameter containing contributions of both volumetric damage and shear damage while the form of the GTN yield function is retained.

Nahshon and Hutchinson (2008) claimed that f is no longer directly tied to the plastic volume change but rather should be regarded as a damage parameter, and introduced an additional term in the evolution equation of f to account for shear damage. Xue directly introduced a new damage parameter, D, which contains both void damage and shear induced damage, and substituted the $q_1 f$ term in Eq. (1) with D. The modified yield function can be expressed as

$$\Phi = \left(\frac{\sigma_e}{\sigma_M}\right)^2 + 2D \cosh\left(\frac{q_2}{2}\frac{\sigma_{kk}}{\sigma_M}\right) - 1 - D^2 = 0, \tag{8}$$

which is in the same form as the original GTN model given by Eq. (1) with $D = q_1 f$.

In establishing shear damage evolution law, both Xue (2008) and Nahshon and Hutchinson (2008) first derived the evolution of shear damage under the pure shear or simple shear state, then extended it to other stress states by introducing a Lode angle dependent function. Nahshon and Hutchinson proposed a phenomenological shear damage law that assumes linear dependence on the porosity and the effective strain increment. Inspired by the solution for coalescence of holes in a shear band by McClintock et al. (1966), Xue developed his shear damage law based on the change of the void ligament of a unit cell model under simple shear deformation. The damage evolution law can be summarized as follows, where (9a) represents the Nahshon–Hutchinson model and
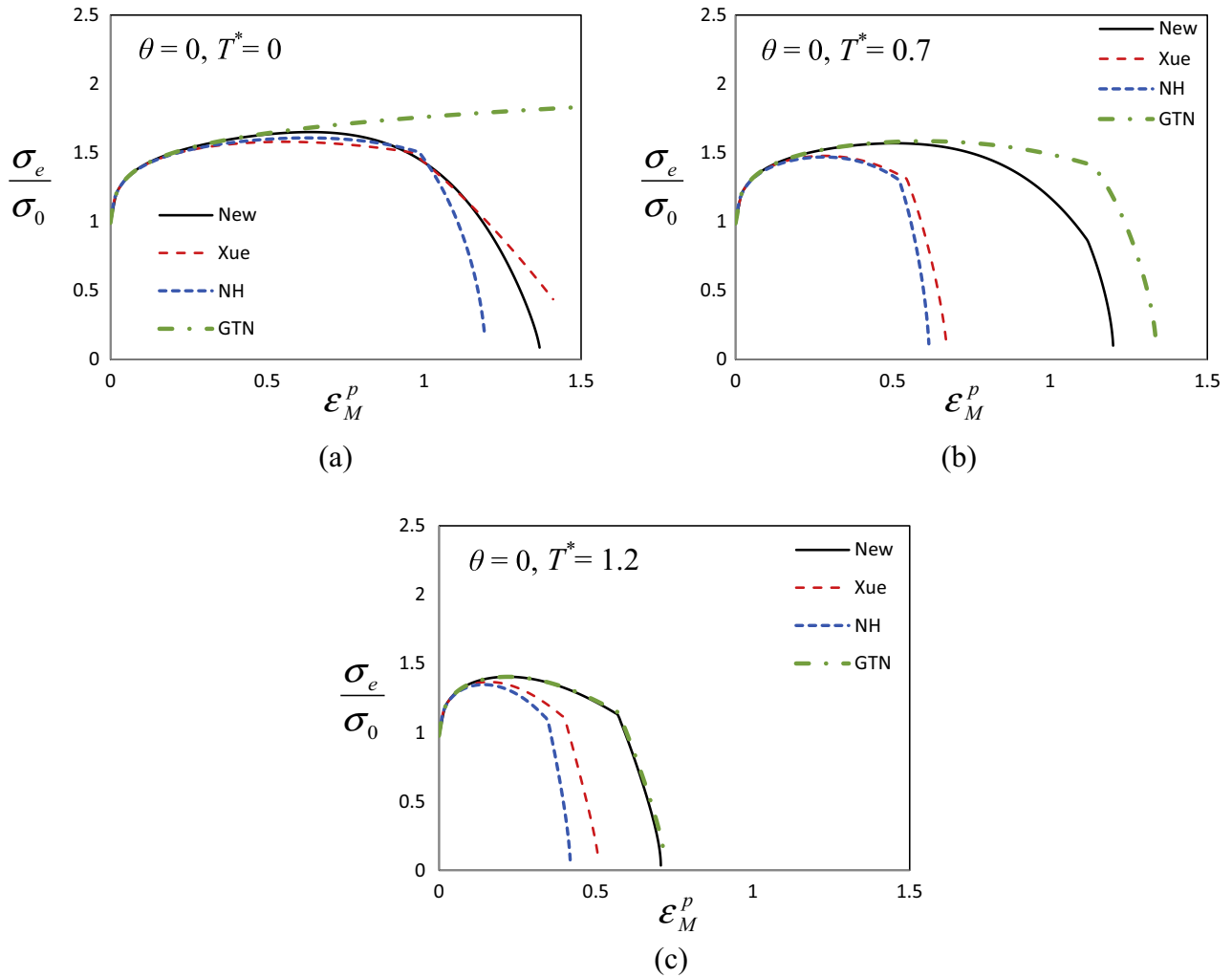
Fig. 3. Comparison of the effective stress vs. matrix plastic strain response between the current model (New), the Xue model, the Nahshon–Hutchinson model (NH), and the GTN model under generalized shear condition with different stress triaxialities.

(9b) represents the Xue model, and (9c) show the Lode angle dependent functions

$$\dot{f} = \dot{f}_g + \dot{f}_n + \dot{f}_s, \quad \dot{f}_s = k_\omega f \omega(\sigma_{ij}) \frac{\sigma_{ij}\dot{\varepsilon}_{ij}^p}{\sigma_e}, \qquad (a)$$

$$\dot{D} = q_1(\dot{f}_g + \dot{f}_n) + \dot{D}_s, \quad \dot{D}_s = q_3 f^{q_4} g(\theta) \varepsilon_M^p \dot{\varepsilon}_M^p, \qquad (b) \qquad (9)$$

$$\omega(\sigma_{ij}) = 1 - [\cos(3\theta + \pi/2)]^2, \quad g(\theta) = 1 - \frac{6|\theta|}{\pi}. \quad (c)$$

Here, θ represents the Lode angle defined as

$$\theta = \tan^{-1}\left[\frac{1}{\sqrt{3}}\left(2\frac{s_2 - s_3}{s_1 - s_3} - 1\right)\right], \qquad (10)$$

with s_1, s_2 and s_3 being the maximum, intermediate, and minimum principal deviatoric stress components. The Lode angle can be related to the third invariant of the deviatoric stress tensor J_3 through $\cos(3\theta + \pi/2) = 27J_3/(2\sigma_e)$.

The shear damage evolution laws of both models share three common features. First, shear damage is a weighted integration of equivalent plastic strain increment (the fraction in the Nahshon and Hutchinson model can be regarded as a definition of the equivalent plastic strain increment). Second, the Lode angle dependency functions, $\omega(\sigma_{ij})$ and $g(\theta)$, have the same limit values. It equals to one at the generalized shear (pure shear state + hydrostatic state) and zero at the generalized tension/compression (uniaxial

tension/compression + hydrostatic state). Third, one material parameter, k_ω or q_3, is used to scale the shear damage growth rate. This parameter can be calibrated using experimental data obtained from a shear dominated test.

The major difference between the two models is the void volume dependency. There is an additional parameter q_4 in Xue's model, where shear damage is scaled by f^{q_4}. The value of q_4 is 1/2 for 2D problem and 1/3 for 3D problem. This parameter has a significant effect on the predicted shear damage since porosity f can vary significantly during the loading history.

Since the model has one generalized damage parameter in Eq. (8), the onset of localization and the final material failure process can be modeled by introducing a D^* in a similar fashion as the f^* concept described in Eq. (6).

2.3. Drawbacks of the existing models

Although the above models have shown improvements in the prediction of shear dominated failure at zero or low, positive triaxiality stress states, it has been observed that these models have inherent drawbacks (Nielsen and Tvergaard, 2009; Malcher et al., 2012). In particular for combined stress states, the prediction of the location of fracture, the displacement to fracture, and the equivalent plastic strain to fracture are not representative of experimental results. As discussed by Nielsen and Tvergaard (2009), the
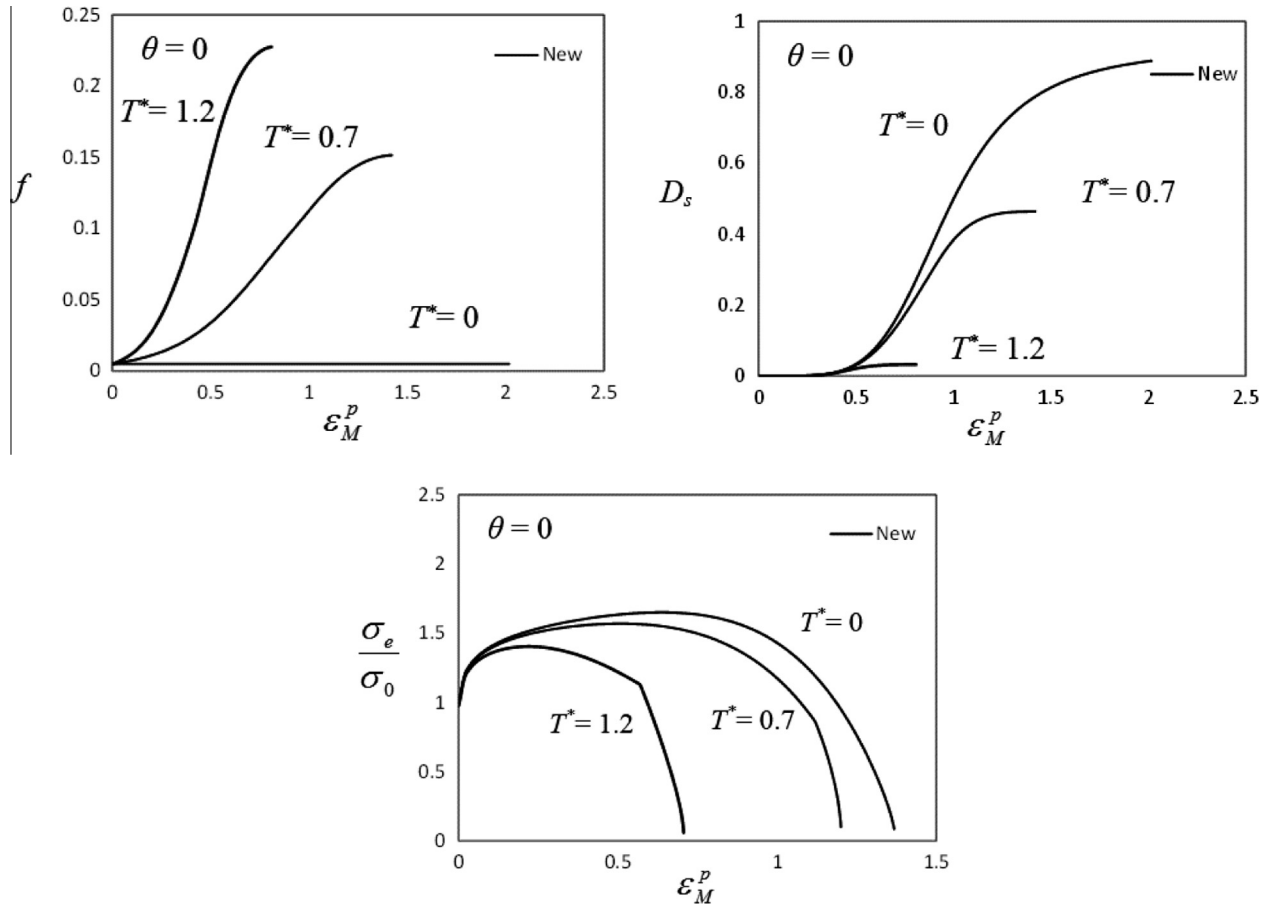
Fig. 4. The predicted (a) void volume fraction vs. matrix plastic strain, (b) shear damage vs. matrix plastic strain and (c) effective stress vs. matrix plastic strain responses by the new model at three triaxiality levels.

additional damage contribution due to the shear modification may have a too strong of an effect in some cases where the stress triaxiality is not low. To solve this problem, Nielsen and Tvergaard (2009) modified the Nahshon–Hutchinson model by pre-multiply an additional stress dependent factor, $\Omega(t)$, on the shear damage term in the Eq. (9a). This $\Omega(t)$ factor is introduced to interpolate between the value one at a low stress triaxiality level, T_1^*, and the value zero at a high stress triaxiality level, T_2^*, with a linear function $\Omega(t) = (T^* - T_2^*)/(T_1^* - T_2^*)$ between the two limits. This modification gives no shear damage when stress triaxiality exceeds the cutoff value. Although this modification can address the shear damage over-prediction problem at high triaxialities discussed in Section 2.2, it bypasses the intrinsic causes of the problem.

In the following, the causes of the limitations for the existing modified GTN models are discussed extensively.

2.3.1. Use of a unified single damage parameter in the yield function

In the original Gurson model, the void coupled yield function is derived from the void deformation behavior in a matrix material. Therefore f represents the physical void volume fraction, and the plastic volume change of the material is due to the void size change. This basis was kept when the Gurson model was extended to the GTN model. The incorporation of shear damage in the modified model was accomplished through the introduction of an additional term in the evolution equation of void volume fraction. This term does not represent a physical value of the porosity but ensures the detrimental effect of void distortion and inter-void linking. However, it is questionable that shear damage has the same significant effects on plastic flow under hydrostatic tension

as porosity has. Since a single scalar damage variable is used to measure the total accumulation of different types of damage, it should not be used as same as the void volume fraction f, in the original yield function. Furthermore, the plastic volumetric strains predicted by Eq. (8) are too large compared to the original GTN model when D_s is high.

Assuming an incompressible matrix material and the associated flow rule, the plastic volume change can be obtained as

$$\dot{\varepsilon}_{kk}^p = \dot{\lambda} 3D \frac{q_2}{\sigma_M} \sinh \left(\frac{q_2}{2} \frac{\sigma_{kk}}{\sigma_M} \right), \tag{11}$$

The plastic multiplier $\dot{\lambda}$ can be derived from the consistency condition, and the void growth rate is determined by Eq. (4).

From the above equation, shear damage contributes to the plastic volume change, and therefore the void growth rate. This results in significant overestimates of volume change predictions, which in turn lead to overestimates of void growth. This implicit coupling serves as one of the main reasons for the over-predicted damage under high triaxiality.

The models also result in unrealistic plastic volume change especially when the stress history is complex. For example, if the material has an initial porosity f_0 and is first subjected to a pure shear loading, the shear damage D_s will increase but the total volume will remain unchanged. If the material is then subjected to a pressure loading, the volume will immediately shrink at a rate above the rate suggested by the initial void volume fracture. The total volume can shrink beyond $(1 - f_0)V_0$ because $D > 0$ at $f = 0$, Eq. (11), where V_0 represents the initial volume.
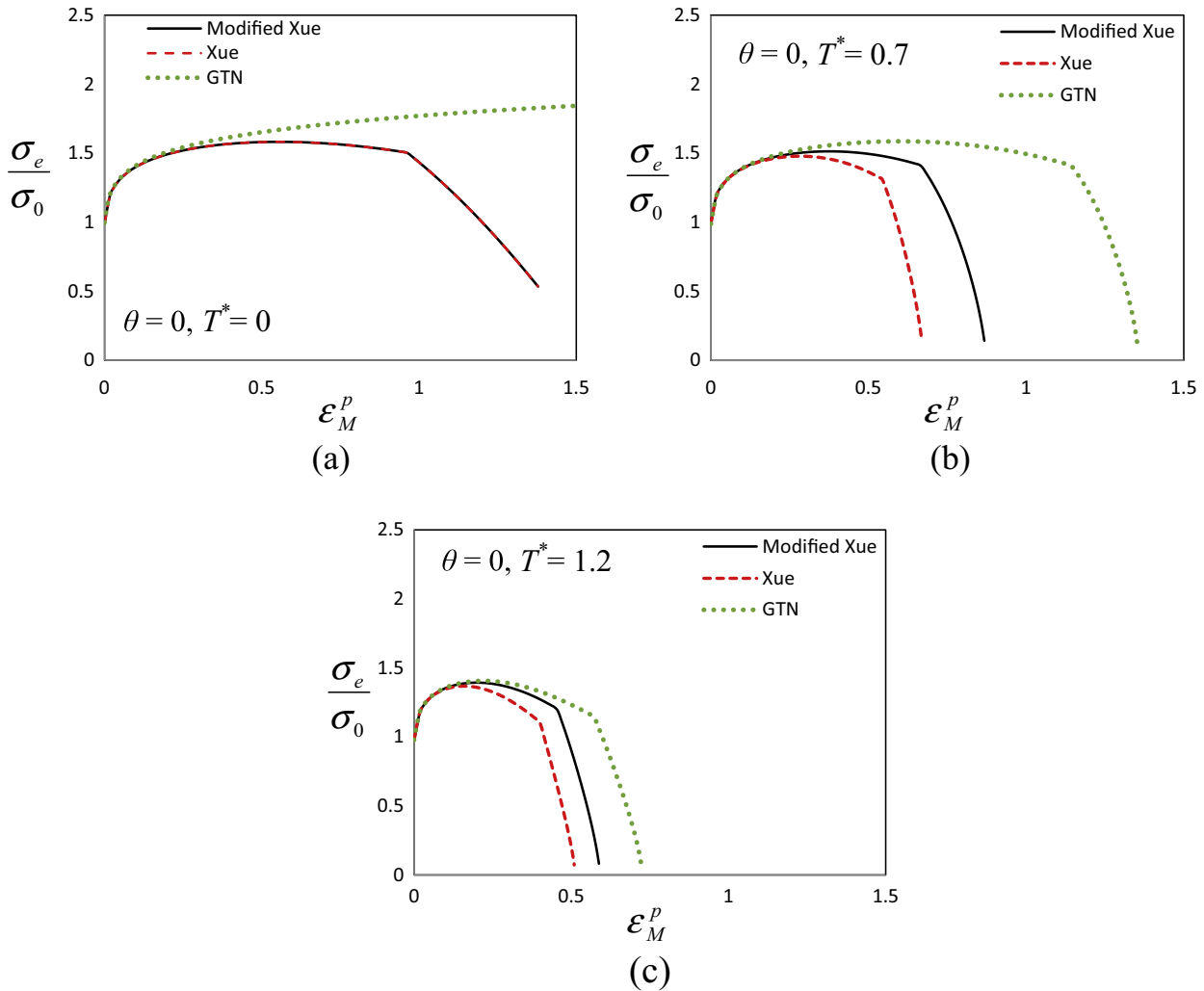
Fig. 5. Comparison of the effective stress vs. matrix plastic strain response between the modified Xue model and the original Xue model under generalized shear condition with different stress triaxialities.
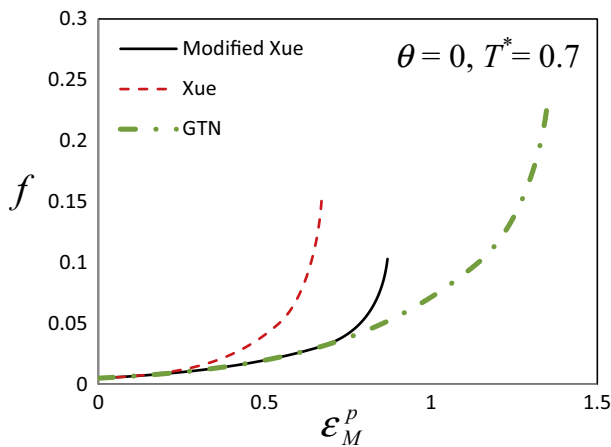

Fig. 6. Comparison of the void growth rates predicted by the modified Xue model, the original Xue's model and the GTN under $\theta = 0$ and $T^* = 0.7$.

The above discussion suggests that the two failure mechanisms, volumetric damage and shear damage, cannot be adequately described using a single damage parameter in the yield function.

2.3.2. The Lode angle dependency

A Lode angle dependent function is used to distinguish the axisymmetric tension state and the pure shear state. The original GTN model provides good prediction at high triaxiality and no damage under pure shear, thus the Lode angle dependent function is taken to be zero for axisymmetric tension and one for pure shear. Xue (2008) showed the ability of his modified GTN model to predict cup–cone fracture of the round bar tensile test and slant fracture of a $C(T)$ specimen, indicating the necessity of the inclusion of the Lode angle dependency in the model.

However, the Lode angle dependent functions used in the existing models preclude failure at generalized tension or generalized compression with zero pressure. From the viewpoint of void ligament reduction, at these stress states, the shortest ligament distance can also be reduced under proportional loading without void volume change. Therefore, the Lode angle function needs to have a non-zero value to predict failure under zero or negative triaxiality.

2.3.3. Dependency of the shear damage on void size

Under the shear deformation field, the voids tend to distort, rotation and may become crack-like, which reduces the ligament distance and results in coalescence. This so called void shearing effect has been studied by many authors. Most of these studies
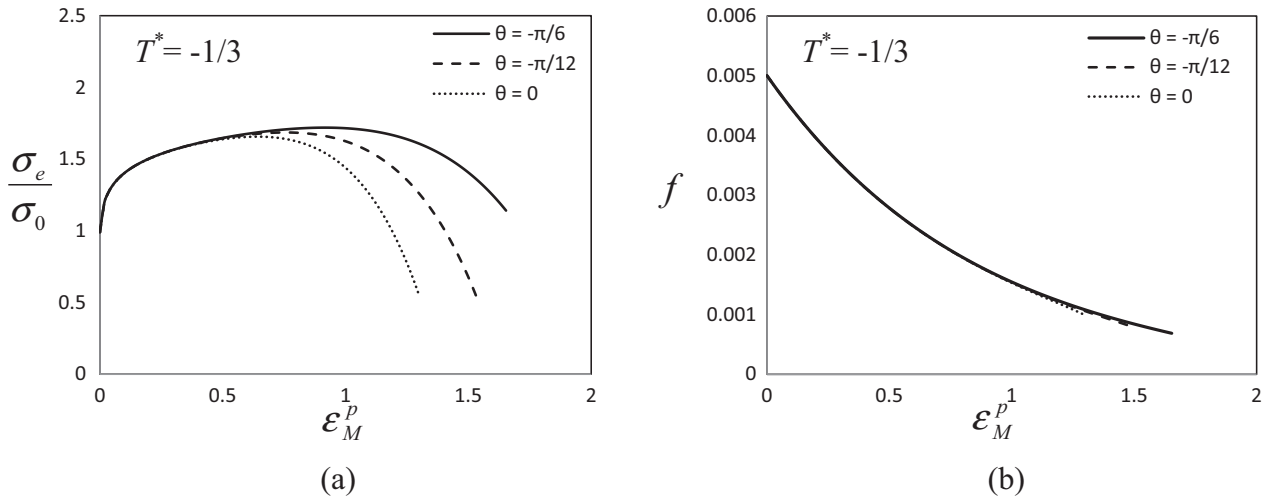
Fig. 7. Predicted effective stress vs. matrix plastic strain and void volume fraction vs. matrix plastic strain responses under negative stress triaxiality ($T^* = -1/3$) and different Lode angles.

Table 2
Nominal chemical composition of Zircaloy-4 (wt%).

Element	Fe	Sn	Cr	O	Zr
Composition	0.21	1.53	0.11	0.13	Balance

were based on finite element analyses of unit cells, e.g., Tvergaard (2008, 2009), and showed the influence of void size on the void shearing effect. Anderson et al. (1990) conducted studies of cells containing micro-cracks under shear deformation field and found that micro-cracks would rotate and align in the preferred direction, resulting in the reduction of the ligament distance and promoting "crack coalescence". However, a quantitative relationship between void size and shear damage is hard to obtain. Moreover, effects of other factors, such as void distribution and void shape, make the problem even more complicated.

The simple linear relationship between shear damage and void volume fraction used by Nahshon and Hutchinson could be another reason it over-predicts the shear damage under high triaxiality. The power parameter q_4 used by Xue gives a better way to

tackle this issue. Since the unit cell model Xue made to determine q_4 may not be valid in reality, it may be better to relax q_4 to a free parameter.

Due to the difficulties mentioned above, to make the problem tractable we take a phenomenological approach assuming shear damage only depends on the stress state and equivalent strain. Further studies are required to obtain a more accurate model.

2.4. The proposed model

To overcome the above drawbacks, we propose a new, extended GTN model. By combining the damage mechanics concept of Lemaitre (Lemaitre, 1985; Lemaitre and Lippmann, 1996) with the Gurson-type void growth model, shear damage in the new model only affects the deviatoric stress while the only cause of the plastic volume change is the porosity.

2.4.1. A new yield function with two damage parameters

In Lemaitre's damage mechanics model, a scalar damage parameter D is defined to represent the general loss of load bearing area, which is coupled in the plasticity model. The loss of load
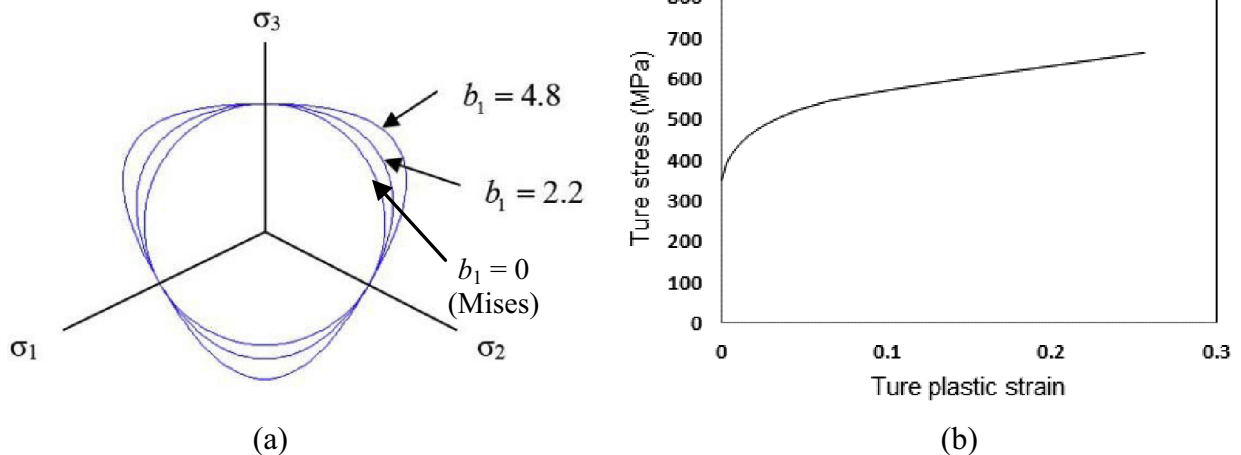

Fig. 8. (a) Yield surface of the matrix material as b_1 takes different values, (b) tensile stress–strain curve.
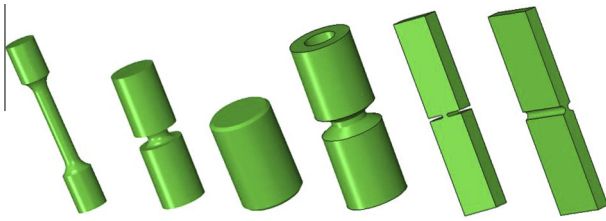
Fig. 9. Sketches of a smooth round bar, a notched round bar, a compression specimen, a torsion specimen, a flat notched tensile specimen, and a flat grooved plane strain specimen.

carrying capacity due to damage is reflected in both the yield function and the elastic stiffness. In the yield function, the effective

stress is scaled by $1/(1-D)$, i.e., $\Phi = \frac{\sigma_e}{1-D} - \sigma_M$. When D equals unity, the material is said to have completely failed.

In the original GTN model, Eq. (1), if no pressure (hydrostatic stress) exists, the yield function can be written as

$$\Phi = \left(\frac{\sigma_e}{\sigma_M}\right)^2 + 2q_1 f - 1 - (q_1 f)^2 = \left(\frac{\sigma_e}{\sigma_M}\right)^2 - (1 - q_1 f)^2. \tag{12}$$

By replacing $q_1 f$ with D, Eq. (12) is equivalent to the Lemaitre model. Since f represents the void volume fraction, $q_1 f$ can be considered as a parameter which quantifies the void damage.

Under a deviatoric stress state, shear damage, D_s, accumulates in the material. If we assume the shear damage only affects the deviatoric stress, and the total damage is the combination of void damage and shear damage, we can add a D_s term in Eq. (12). Therefore, the yield function without pressure can be modified as

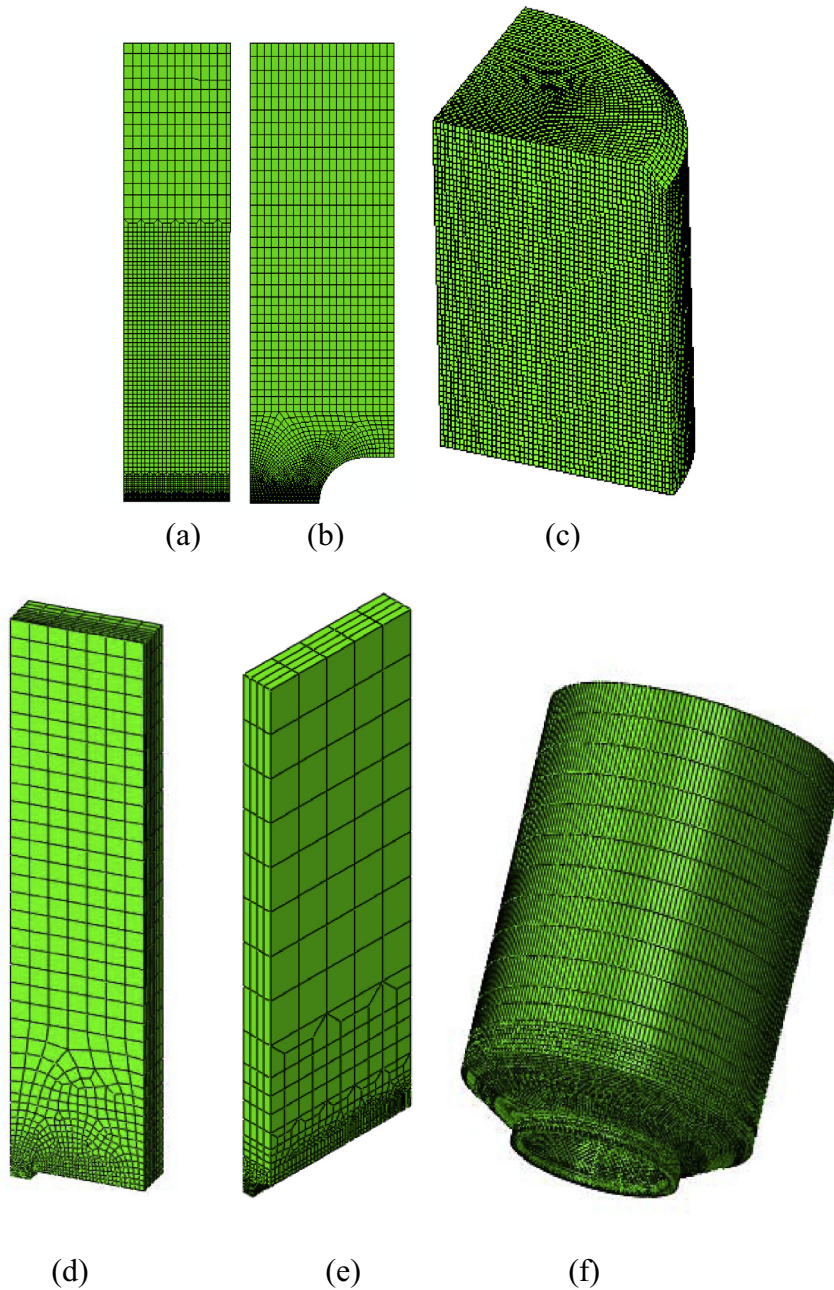

(a) (b) (c)

(d) (e) (f)

Fig. 10. Finite element mesh of (a) a smooth round tensile specimen, (b) a notched round tensile specimen, (c) a compression specimen with $L/D = 1.5$, (d) a flat notched tensile specimen, (e) a flat grooved plane strain tensile specimen, and (f) a pure torsion specimen.

Table 3
Model parameters for Zircaloy-4.

q_1	q_2	f_0	f_n	S_n	ε_n	f_c	f_f	ε_f^s	n	k
1.5	1	0	0.012	0.02	0.1	0.03	0.08	0.5	5	0.5

$$\Phi = \left(\frac{\sigma_e}{\sigma_M}\right)^2 - (1 - q_1 f - D_s)^2$$

$$= \left(\frac{\sigma_e}{\sigma_M}\right)^2 + 2q_1 f + 2D_s - \left[1 + (q_1 f + D_s)^2\right]. \qquad (13)$$

Under a general stress state, a void will grow due to hydrostatic stress. Assuming the softening effect due to void growth takes the same form as given in the original GTN model, the yield function of a new, extended GTN model can be expressed as

$$\Phi = \left(\frac{\sigma_e}{\sigma_M}\right)^2 + 2q_1 f \cosh\left(\frac{q_2}{2}\frac{\sigma_{kk}}{\sigma_M}\right) - \left[1 + (q_1 f + D_s)^2 - 2D_s\right] = 0. \qquad (14)$$

When the total damage ($q_1 f + D_s$) becomes unity, the material loses its load carrying capacity completely. The new model degenerates to the GTN model when no shear damage exists and it becomes the same form as the CDM of Lemaitre when the material is under pure shear.

This new model separates contributions from the two failure mechanisms, i.e., volumetric damage and shear damage. Fig. 1 shows the effect of the volumetric damage and shear damage on the yield surface. In Fig. 1(a), where $D_s = 0$, the model reduces to the GTN model and the yield surface shrinks as $q_1 f$ increases. When $q_1 f$ becomes one, the yield surface shrinks to a point. In Fig. 1(b) is shown the additional softening effect provided by the shear damage. For a given value of $q_1 f$, the yield surface shrinks as D_s increases.

2.4.2. The shear damage evolution law

The shear damage evolution law, which features potential contributions from several failure mechanisms, might be fairly complex and the preliminary studies conducted by the authors attempt to balance the accuracy of the model and the number of material parameters to be calibrated. A quantitative relationship between void size and shear damage has not been firmly established since shear localization can occur with or without the existence of voids. In the material considered in this study (Zircaloy-4), we assume that shear damage is not directly linked to the void volume fraction, and regard void growth as merely one of the sources that weakens the material under shear loading.

Here a phenomenological approach is taken and it is assumed that ductile damage is due to accumulation of plastic deformation.
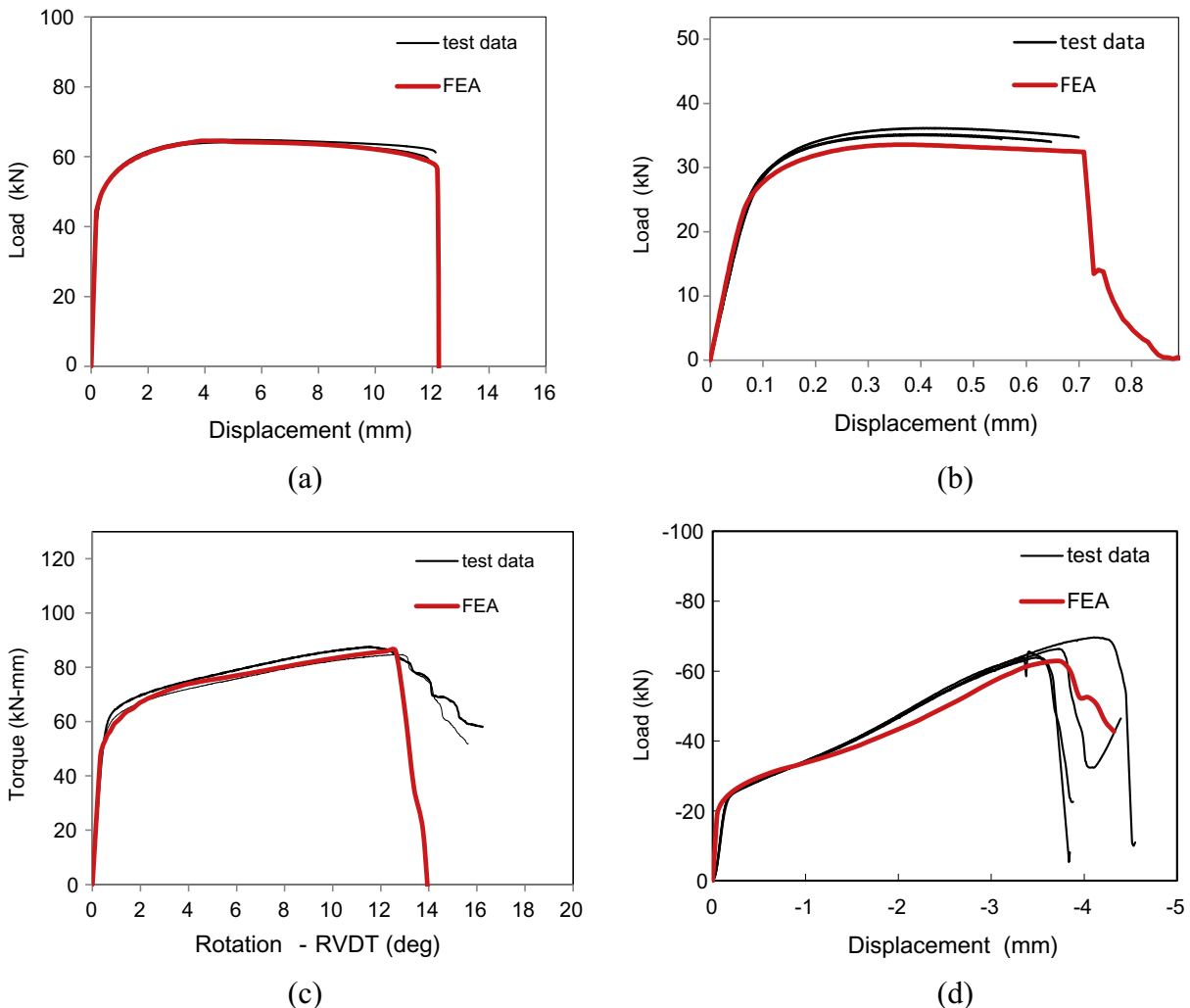
Fig. 11. Comparison of load vs. displacement or torque vs. twist angle response between the experimental data and FEA prediction: (a) smooth round tensile specimen; (b) notched round tensile specimen; (c) pure torsion specimen; (d) compression specimen.
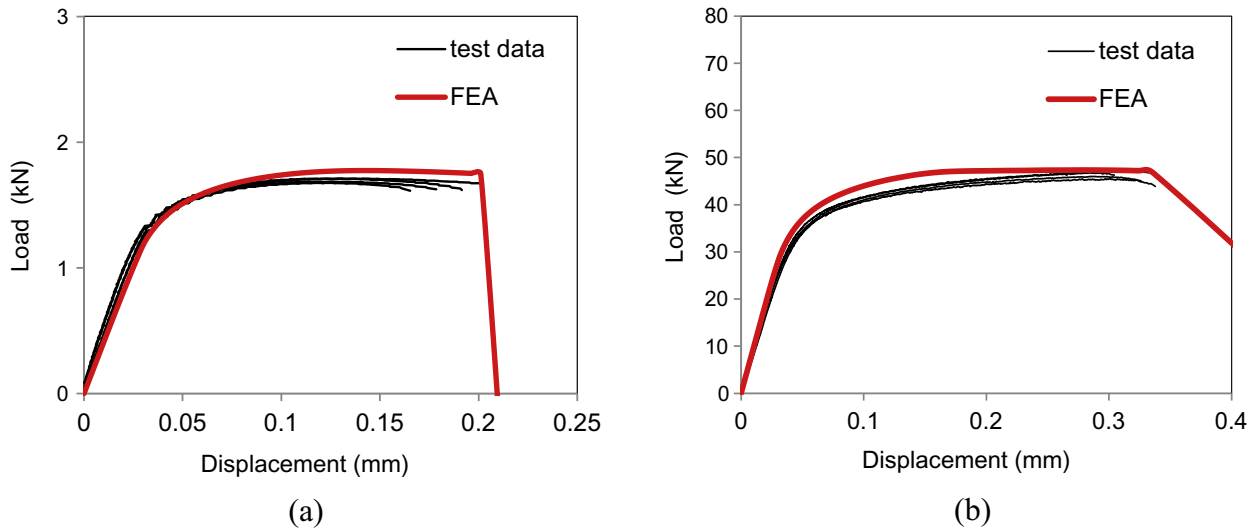
Fig. 12. Comparison of the computed load vs. displacement responses with experimental data for (a) flat notched tensile specimen and (b) flat grooved plane strain tensile specimen.
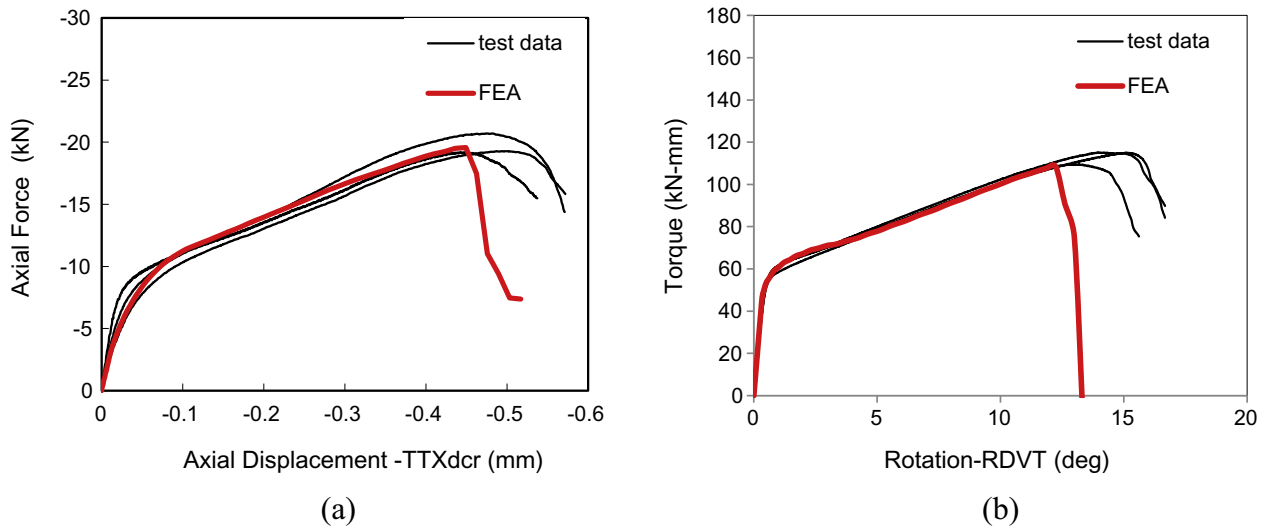

Fig. 13. Comparisons between the numerical predictions and the experimental data of the torsion–compression specimen: (a) axial force vs. axial displacement; (b) torque vs. twist angle.

Consequently, the shear damage is taken to be a function of plastic strain and stress state. Let ε_f^s be the failure strain under the pure shear state. A shear damage parameter can be defined by a power function as below

$$D_s = \left(\frac{\varepsilon_M^p}{\varepsilon_f^s}\right)^n, \tag{15}$$

where ε_M^p represents the matrix plastic strain and n is a weakening exponential larger than one. D_s is equal to one when ε_M^p reaches to ε_f^s. With n is greater than one, the softening effect is small at the early stage of plastic deformation and becomes larger as the material approaches failure. The incremental form of shear damage can be expressed as

$$\dot{D}_s = \frac{n D_s^{\frac{n-1}{n}}}{\varepsilon_f^s} \dot{\varepsilon}_M^p. \tag{16}$$

To extend Eq. (16) to any arbitrary stress state, a function of triaxiality T^* and Lode angle is introduced as a weight factor (Xue, 2007; Gao et al., 2010; Zhou et al., 2012)

$$\dot{D}_s = \psi(\theta, T^*) \frac{n D_s^{\frac{n-1}{n}}}{\varepsilon_f^s} \dot{\varepsilon}_M^p, \tag{17}$$

where the weight function $\psi(\theta, T^*)$ must have unit value under pure shear state. To our knowledge, there is no generally accepted form of this function at present. In this study, the weight function is taken to be the same as the $g(\theta)$ function used in the Xue model (2008) for positive stress triaxiality (Eq. (9c)). A modification is made to provide the ability of predicting shear damage as $\theta = \pm\pi/6$ with negative stress triaxiality

$$\psi(\theta, T^*) = \begin{cases} g(\theta) & T^* > 0 \\ g(\theta)(1-k) + k & T^* \leqslant 0 \end{cases}, \tag{18}$$

where the constant k in (18) represents the value of the weight factor when the stress triaxiality is negative and $\theta = \pm\pi/6$, which can be calibrated using axisymmetric compression test data. In the Xue model and the Nahshon–Hutchinson model, shear damage is indirectly related to the stress triaxiality through the void volume fraction dependency. For the material (Zircaloy-4) considered in this study, it is found that Eq. (18) provides an adequate description of
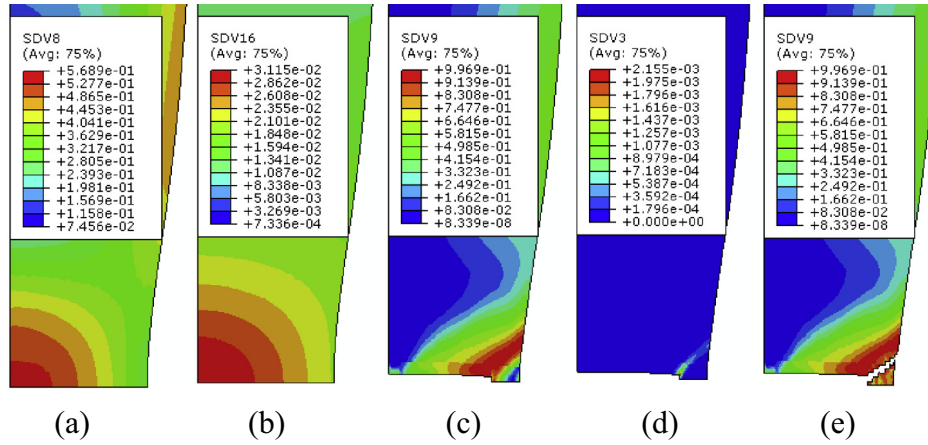
Fig. 14. Crack initiation and growth in the smooth round tensile specimen: (a) contour plot of triaxiality before fracture initiation; (b) contour plot of porosity before fracture initiation; (c) contour plot of the weight function after some amount of crack propagation; (d) contour plot of shear damage after some amount of crack propagation; (e) final fracture.

the stress state effect on shear damage. While the rather simplified form of the weight function given by Eq. (18) works reasonably well for the material considered in this study by being able to capture the damage evolution process in various specimens and reproduce the experimental data, further investigation needs to be dedicated to explore different forms of the $\psi(\theta, T^*)$ function.

2.4.3. Evolution of volumetric damage

The volumetric damage is due to the increase of void volume. The evolution equation for void volume fraction is the same as in the original GTN model described in Section 2.1.

2.4.4. Separate critical conditions for the two types of damage

The critical damage conditions play a significant role in the prediction of failure initiation and propagation. After the critical condition is reached, damage increases rapidly and the softening process accelerates so that material loses its load carrying capacity quickly.

For the two kinds of damage discussed above, when triaxiality is high, volumetric damage (increase of void volume) triggers coalescence, but when triaxiality is low, shear damage often triggers failure initiation. Unlike the previous model with only one critical damage condition, a separate critical damage condition can be established for each damage mechanism. Under the situation that void damage grows faster than shear damage, the porosity reaches the critical value first and triggers void coalescence, and vice versa. The competition between the two failure mechanisms, influenced significantly by the stress state, results in a different mode of fracture and different appearance of the fracture surface.

In this study, void coalescence is modeled the same way as described in Section 2.1 using the f^*-function. The shear damage evolution law is selected so that the damage acceleration effect is already reflected. For common ductile metals and alloys, the softening induced by shear damage increases slowly when the plastic strain is small and accelerates when ε_M^p approaches ε_f^s, so the n-power in the shear damage definition is usually greater than 4. The parameters ε_f^s and n determines the onset of shear localization.

2.4.5. Summarization of the extended GTN model

The following equations summarize our extended GTN model

$$\Phi = \left(\frac{\sigma_e}{\sigma_M}\right)^2 + 2q_1 f^* \cosh\left(\frac{q_2}{2}\frac{\sigma_{kk}}{\sigma_M}\right) - \left[1 + (q_1 f^* + D_s)^2 - 2D_s\right] = 0;$$

$$\dot{\varepsilon}_{ij}^p = \dot{\lambda} n_{ij}; \quad n_{ij} = \frac{\partial \Phi}{\partial \sigma_{ij}},$$

$$\dot{f} = \dot{f}_g + \dot{f}_n; \quad \dot{f}_g = (1-f)\dot{\varepsilon}_{kk}^p; \quad \dot{f}_n = A_N \dot{\varepsilon}_M^p;$$

$$A_N = \frac{f_n}{S_n\sqrt{2\pi}} \exp\left[-\frac{1}{2}\left(\frac{\varepsilon_M^p - \varepsilon_n}{S_n}\right)^2\right];$$

$$f^* = \begin{cases} f & \text{for} \quad f \leqslant f_c \\ f_c + \frac{1/q_1 - f_c}{f_f - f_c}(f - f_c) & \text{for} \quad f_c \leqslant f \leqslant f_f \end{cases};$$ (19)

$$\dot{D}_s = \psi(\theta, T^*)\frac{nD_s^{\frac{n-1}{n}}}{\varepsilon_f^s}\dot{\varepsilon}_M^p; \quad \psi(\theta, T^*) = \begin{cases} g(\theta) & T^* > 0 \\ g(\theta)(1-k) + k & T^* \leqslant 0 \end{cases},$$

$$D = q_1 f^* + D_s; \quad \sigma_{ij}\dot{\varepsilon}_{ij}^p = (1 - D/q_1)\sigma_M \dot{\varepsilon}_M^p.$$

Compared to the original GTN model, the new model introduces the following additional parameters: the new state variable D_s (shear damage parameter), the weight function ψ, the total damage D, and three new material constants, the weakening exponential n, the failure strain under pure shear ε_f^s and the weight factor k under negative triaxiality. When D reaches unity, the material is said to have completely failed. Based on the concept of CDM, stresses in the material increase due to the reduction of the effective load bearing area resulted from damage. This should be reflected in the equation describing the equivalence of the rates of macroscopic plastic work and the matrix plastic dissipation. The $(1 - D/q_1)$ factor used in Eq. (19) ensures the model can degenerate to the GTN model as $D_s = 0$.

2.5. Matrix plasticity behavior

For an isotropic material in general, the yield function and flow potential should be functions of the hydrostatic stress as well as the second and third invariant of the deviatoric stress tensor, J_2 and J_3 (Gao et al., 2011 and references therein). If the material exhibits no pressure sensitivity or Lode dependency, the J_2 flow theory is usually used to describe the plastic response. In the original GTN model, the matrix plasticity behavior follows the J_2 flow plasticity theory, where the equivalent stress σ_e is the von Mises stress defined as $\sigma_e = \sqrt{3J_2}$.

3. Single material point test

To illustrate the effect of the modifications presented above on the predicted material behavior, a series of numerical tests are presented in this section and the results are compared with the original GTN model as well as the Xue model and Nahshon–Hutchinson model.

3.1. Analysis procedure

For proportional loading histories, the stress tensor can be represented by a load proportionality factor $\tilde{\sigma}$ multiplied by a constant tensor R_{ij}. The designated stress triaxiality and Lode parameter can be obtained by choosing appropriate R_{ij} values.

A load-controlled process using $\tilde{\sigma}$ as the loading parameter is difficult to achieve because of the softening effect. Instead, an algorithm is developed to apply the plastic multiplier incrementally and compute $\tilde{\sigma}$ and the internal variables ε_M^p, f and D_s at each step accordingly.

To illustrate this process, we started with the consistency condition

$$\dot{\Phi} = \frac{\partial \Phi}{\partial \sigma_{ij}} \dot{\sigma}_{ij} + \frac{\partial \Phi}{\partial \sigma_M} \frac{\partial \sigma_M}{\partial \varepsilon_M^p} \dot{\varepsilon}_M^p + \frac{\partial \Phi}{\partial f^*} \frac{\partial f^*}{\partial f} \dot{f} + \frac{\partial \Phi}{\partial D_s} \dot{D}_s = 0, \quad (20)$$

where the rates of internal variables ε_M^p, f and D_s can be written as functions of λ. Substituting $\dot{\varepsilon}_M^p$, $\dot{f}$ and $\dot{D}_s$ in (20) results in

$$\dot{\lambda} = \frac{1}{H} \frac{\partial \Phi}{\partial \sigma_{ij}} \dot{\sigma}_{ij}, \quad (21)$$

where H is the hardening modulus

$$H = -\left(\frac{\partial \sigma_M}{\partial \varepsilon_M^p} \frac{\partial \Phi}{\partial \sigma_M} \frac{\partial \varepsilon_M^p}{\partial \lambda} + \frac{\partial \Phi}{\partial f^*} \frac{\partial f^*}{\partial f} \frac{\partial f}{\partial \lambda} + \frac{\partial \Phi}{\partial D_s} \frac{\partial D_s}{\partial \lambda} \right). \quad (22)$$

For a given stress state where the ratios between stress components are fixed, Eq. (21) can be written as (23a) and the increment of $\tilde{\sigma}$ can be obtained by (23b)

$$\dot{\lambda} = \frac{\dot{\tilde{\sigma}}}{H} \frac{\partial \Phi}{\partial \sigma_{ij}} R_{ij} \quad \text{(a)}, \\ \dot{\tilde{\sigma}} = \frac{H}{\frac{\partial \Phi}{\partial \sigma_{ij}} R_{ij}} \dot{\lambda} \quad \text{(b)}. \quad (23)$$

Eq. (23b) can be solved numerically. This is done in MATLAB using a forward Euler integration scheme. The increment size is reduced until the solution is converged. The initial values of $\tilde{\sigma}$ at the onset of plastic deformation ($\lambda = 0$) can be solved from Eq. (14).

The details of the procedures described above to maintain the stress triaxiality and Lode parameter at constant values during the loading history are given in Appendix A.

3.2. Numerical examples

In the numerical examples presented in this Section, the matrix material is assumed to follow the J_2 flow plasticity theory and obeys a power-law hardening, true stress–strain relation

$$\begin{cases} \varepsilon = \frac{\sigma}{E} & \sigma \leqslant \sigma_0 \\ \varepsilon = \frac{\sigma_0}{E} \left(\frac{\sigma}{\sigma_0} \right)^N & \sigma > \sigma_0 \end{cases}. \quad (24)$$

Here the material parameters are taken to be $E/\sigma_0 = 300$ and $N = 0.1$, where E, σ_0 and N represent the Young's modulus, yield stress and hardening exponent respectively. The damage related parameters for extended GTN model are listed in Table 1, with no consideration of void nucleation.

For comparisons among the current model and the Xue model, the Nahshon–Hutchinson model, and the original GTN model, the same matrix material constants and volumetric damage parameters are adopted in the numerical analyses. Specific parameters used to define shear damage contribution in the Xue model and the Nahshon–Hutchinson model are chosen to ensure these models predict similar behaviors as the current model under the pure shear condition. The parameters chosen are $k_\omega = 3$ for the Nahshon–Hutchinson model and $q_3 = 1.8$ and $q_4 = 1/3$ for the Xue model.

3.2.1. Effects of parameters n and ε_f^s

Shear damage is an important state variable introduced in the new model and the evolution of shear damage is governed by two materials constants, n and ε_f^s. To understand the effects of n and ε_f^s on model behavior, a material point is analyzed under pure shear loading. In these analyses, various values of n and ε_f^s are considered, while all other model parameters take the values given in Table 1. Fig. 2(a) shows the effect of n on the effective stress vs. matrix plastic strain response, where ε_f^s is taken to be 1.4 and various values of n are considered. A larger n results in a smaller softening effect but leads to a more sudden load drop as the matrix plastic strain approaches to ε_f^s. This confirms that the damage acceleration effect is already reflected in the shear damage evolution law if a large value of n is used. Fig. 2(b) shows the effect of ε_f^s on the effective stress vs. matrix plastic strain response, where $n = 5$ and different values of ε_f^s are considered. A larger ε_f^s value results in a delayed failure initiation. The two parameters n and ε_f^s in the new model work together to define the critical shear damage condition.

3.2.2. Case 1 – comparison of model predictions under generalized shear loading

For generalized tension (uniaxial tension + hydrostatic stress) where $T^* > 0$ and $\theta = -\pi/6$, there is no difference among predicted results from the four models. However, under generalized shear (pure shear + hydrostatic stress) where $\theta = 0$, the models predict different behaviors. Here comparisons are made at three levels of stress triaxialities, $T^* = 0$, 0.7 and 1.2. Fig. 3 shows the effective stress σ_e vs. matrix plastic strain ε_M^p response generated by the four models, where the black solid curve represents the result of the current model and the blue, red and green dash lines represent the results of the Xue model, the Nahshon–Hutchinson model and the GTN model respectively.

For the pure shear case ($\theta = 0$, $T^* = 0$) shown in Fig. 3(a), the predictions of the current model, the Xue model, and the Nahshon–Hutchinson model show little difference prior to shear localization. These three modified GTN models result in similar material softening behavior caused by shear damage. In contrast, the original GTN model does not predict any damage as expected.

The difference between the current model and the other two modified models is apparent as the stress triaxiality increases. Fig. 3(b) displays the results for $T^* = 0.7$ and Fig. 3(c) displays the results for $T^* = 1.2$. Results of the Xue model and the Nahshon–Hutchinson model both predict significantly higher damage than the current model and the GTN model. But as discussed in Section 2.3, the shear damage corrections introduced in the Xue model and the Nahshon–Hutchinson model are too strong at high triaxiality levels. On the other hand, the predicted softening effect by the current model lies between the results from the original GTN model and the Xue and Nahshon–Hutchinson models. As the triaxiality level increases, the predictions of the current model approaches the GTN model. With the new model, shear damage governs the failure behavior when the triaxiality is low. As the triaxiality increases, the dominant failure mechanism shifts to void growth and coalescence. At high triaxiality levels (for $T^* > 1.2$
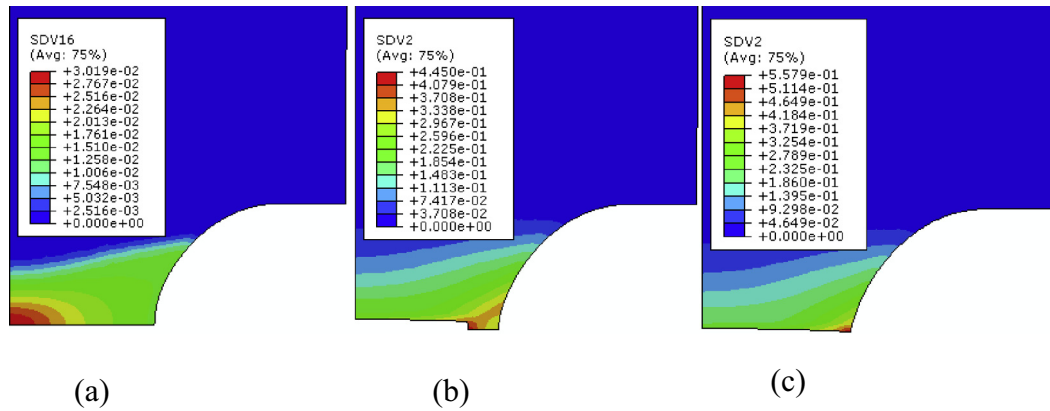
Fig. 15. Crack initiation and growth in the notched round tensile specimen: (a) contour plot of porosity before fracture initiation; (b) contour plot of effective plastic strain after some amount of crack propagation; (c) final fracture.

here), void damage is dominant, and the shear effect is negligible. This also matches findings by numerous researchers that the original GTN model works well under high stress triaxiality conditions.

This transition of damage mechanism can be better observed in Fig. 4(a) and (b), where the evolution of the two damage variables f and D_s is plotted vs. the matrix plastic strain at three triaxiality levels. At $T^* = 0.7$, two damage effects are nearly equal. As T^* increases, the shear damage is taken over by the void damage, the softening behavior becomes more pronounced and the onset of material failure occurs earlier (Fig. 4(c)).

3.2.3. Case 2 – effect of the introduction of two separate damage parameters in the yield function

To illustrate the effect of the introductions of two separate damage parameters in the yield function, we consider a modified Xue model, where the volumetric damage and shear damage parameters present separately in the yield function as shown in Eq. (14), and compare the numerical predictions with the original Xue model. Fig. 5 plots the σ_e vs. ε_M^p responses under generalized shear ($\theta = 0$) for the $T^* = 0$, 0.7, and 1.2 cases, where the results of the modified Xue model, the original Xue's model and the GTN model are displayed in black, red and green lines respectively. For pure shear loading ($T^* = 0$), since the volumetric damage does not grow,

the modified Xue model and the original Xue model become the same, Fig. 5(a). The modified Xue model predicts less softening effect and delayed material failure compared to the original Xue model, Fig. 5(b) and (c). It is worth noting that, unlike the new model developed in this study, the modified Xue model still predicts significant shear damage effect under high stress triaxiality level.

Fig. 6 compares the void growth rates predicted by the modified Xue model, the original Xue's model and the GTN under $\theta = 0$ and $T^* = 0.7$, which clearly indicates that the void growth rate predicted by using Eq. (14) is much slower than the original Xue model. In particular, the modified Xue model predicts almost the same void growth rate as the GTN model in the early stage of loading while the original Xue model predicts a much accelerated void growth rate.

3.2.4. Case 3 – failure under negative stress triaxiality

Under very low or negative stress triaxiality, the void growth mechanism is suppressed, and shear damage becomes the driver for material failure. This case study illustrates the capability of our proposed model to predict damage and failure under these conditions. The loading conditions considered are for $T^* = -1/3$ with three different Lode angles: $\theta = -\pi/6$, $\theta = -\pi/12$, and $\theta = 0$.
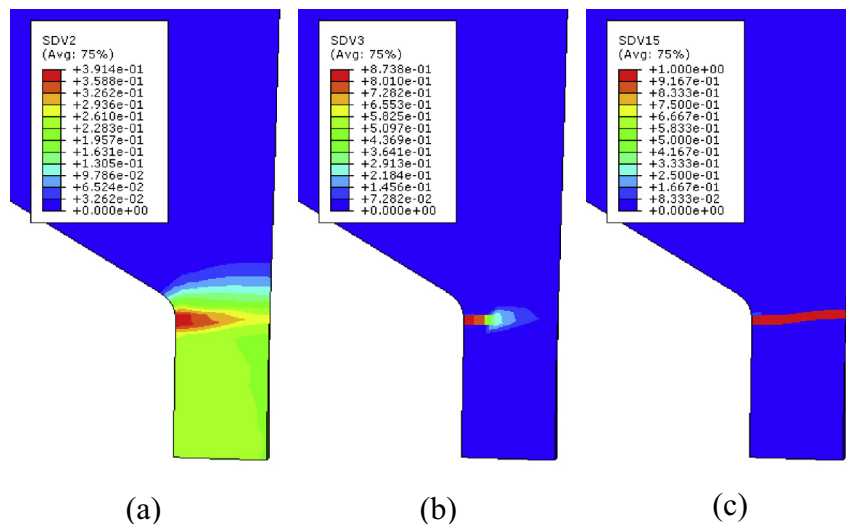

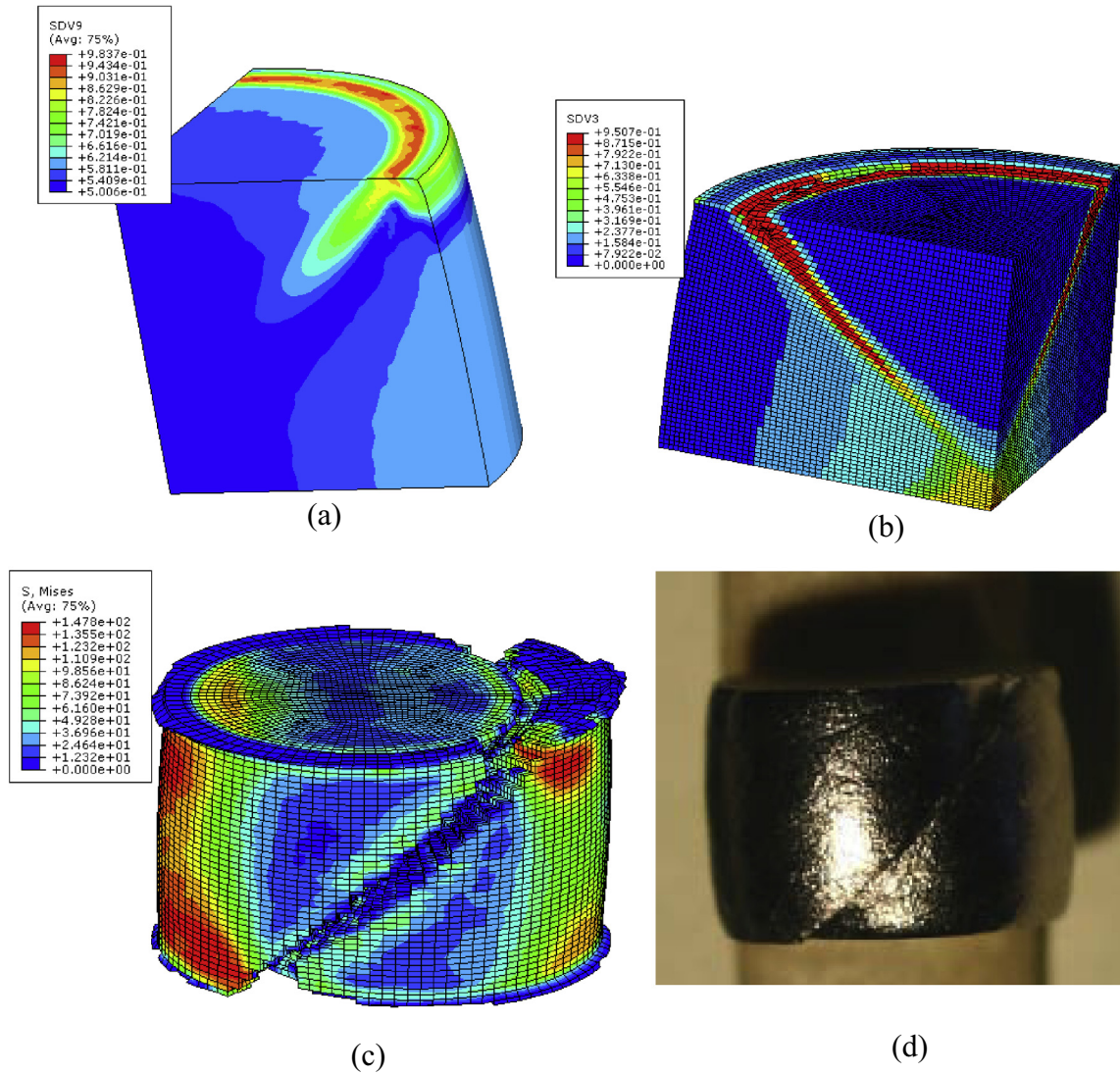**Fig. 16.** Crack initiation and growth in the pure torsion specimen: (a) contour plot of equivalent plastic strain before fracture initiation; (b) contour plot of shear damage before fracture initiation; (c) final fracture.

Fig. 17. Crack initiation and growth in the compression specimen: (a) contour plot of the weight function before fracture initiation; (b) contour plot of shear damage showing slant crack growth from the top of the specimen toward the center of the specimen; (c) slant fracture predicted using a full model with a coarse mesh; (d) photo of a fractured specimen.

The predicted σ_e vs. ε_M^p and f vs. ε_M^p responses are shown in Fig. 7. The model predicts ductile failure even when the triaxiality is negative and the void tends to close (Fig. 7(b)). From Fig. 7(a), the $\theta = -\pi/6$ case gives the highest failure strain while the $\theta = 0$ gives the lowest failure strain. This difference in the predicted ductile failure behavior is determined by the parameter k introduced in Eq. (18).

4. Modeling the ductile fracture behavior of a beta-treated Zircaloy-4

In this section, the newly extended GTN model described above is calibrated for a beta-treated Zircaloy-4 and used to predict damage and fracture of a variety of specimens.

4.1. Material

The beta-treated Zircaloy-4 considered in this study is the same material studied by Zhai et al. (2014) and Zhang et al. (2012). The chemical compositions of this material are listed in Table 2. All the specimens were extracted from wrought material in the

longitudinal direction and tests were conducted at room temperature and quasi-static loading rate. The Zircaloy-4 was heat-treated to produce a random texture on a macroscopic scale and is considered isotropic in this study. The Young's modulus of the material is 99.6 GPa and the Poisson's ratio is 0.34.

A recent study found that the matrix plasticity behavior of this material exhibits tension–compression asymmetry and follows a J_2–J_3 dependent plasticity model (Zhai et al. 2014). According to this model, the definition of equivalent stress is modified as

$$\sigma_e = c_1 \left(3\sqrt{3} J_2^{3/2} + b_1 J_3 \right)^{1/3}, \tag{25}$$

where b_1 is a function of ε_M^p as defined by Eq. (26) and $c_1 = 1/(2b_1/27 + 1)^{1/3}$

$$
\begin{aligned}
b_1 &= 2.2 & \text{when} \quad & \varepsilon_M^p \leqslant 0.1 \\
b_1 &= 17.3 \times (\varepsilon^p - 0.1) + 2.2 & \text{when} \quad & 0.1 < \varepsilon_M^p < 0.2 . \\
b_1 &= 4.8 & \text{when} \quad & \varepsilon_M^p \geqslant 0.2
\end{aligned}
\tag{26}
$$

The varying b_1 gives a distortional hardening effect on the present material. Fig. 8(a) illustrates the shape change of yield surface with the value change of the parameter b_1. When b_1 is zero, the
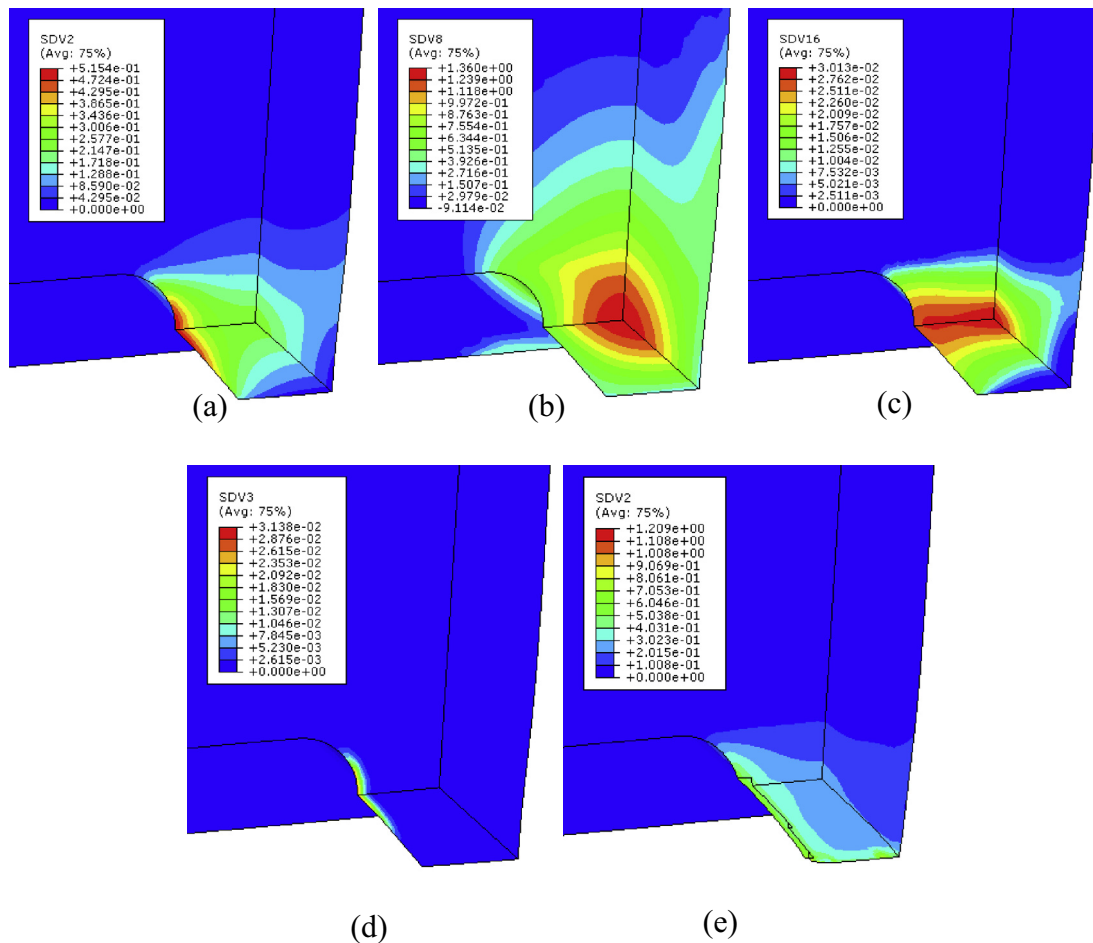
Fig. 18. Crack initiation and growth in the flat notched tensile specimen: (a–d) contour plots of equivalent plastic strain, triaxiality, porosity and shear damage before fracture initiation; (e) final fracture.

model becomes identical to the Mises plasticity model. When b_1 is greater than zero, the yield stress in compression will be larger than the yield stress in tension. Fig. 8(b) shows the stress strain curve of the matrix material under tension. Details of this plasticity model can be found in Zhai et al. (2014).

Although the plasticity behavior of matrix material is complex, the purpose of this section is not to provide a detailed discussion on this subject. The objective of this section is to provide an example of a real-world application of proposed ductile fracture model. From model calibration to numerical prediction, the emphasis is on the ductile fracture behavior. The main story the authors would like to share is the ability of the proposed model to predict failure under various stress states.

Cockeram and Chan (2013) conducted in situ experimental studies over a range of positive stress triaxialities on beta-treated Zircaloy-4 and Zircaloy-2. Several important void formation and damage evolution characteristics observed in their experiments are utilized to determine the material constants in the void model. The material is initially void-free. Fracture is observed as a process of void nucleation, growth and coalescence. The lath boundaries for beta-treated Zircaloy-4 are covered with laves phase particles that are localized sites for void nucleation. Voids are previously observed to nucleate on these precipitates located at lath boundaries. Void nucleation may also occur within the lath at the intersection of slip bands. Void coalescence generally resulted in the formation of larger elongated voids or microcracks. Many lath boundaries were observed to be dotted with rows of micron-sized

voids, whose coalescence eventually would lead to the formation of grain boundary microcracks.

The experimental studies by Cockeram and Chan (2013) also indicate that the critical local strain at the initiation of void nucleation is almost constant for all the stress states studied. The strain to failure is shown to be controlled by the process of void growth and coalescence that is strongly dependent on stress-state.

In the material modeling, we try to correlate the void related material constants to the experimental observation. It must be pointed out though, f should be regarded as an effective void volume fraction, which is not correlated to the actual void size. The void distribution in the material is highly non-homogenous, mainly located along the lath boundaries in the form of micron-sized voids. In the coalescence process, microcracks are formed from the linkage of these small voids.

The initial void volume, f_0, is set to be zero and void nucleation is assumed to be strain-controlled. Cockeram and Chan (2009) found that void nucleation process in the tensile specimens was observed to occur at the UTS and beyond. From the uniaxial tensile tests conducted in this study, the strain value when necking occurs is around 0.1, which can be regarded as the mean strain for void nucleation, ε_n. It was observed that once the voids are nucleated, little growth is required before the voids coalesce. Therefore, we set the critical porosity f_c to be slightly larger than f_n. Other parameters are calibrated by matching the finite element analysis results to experimental obtained load–displacement response.
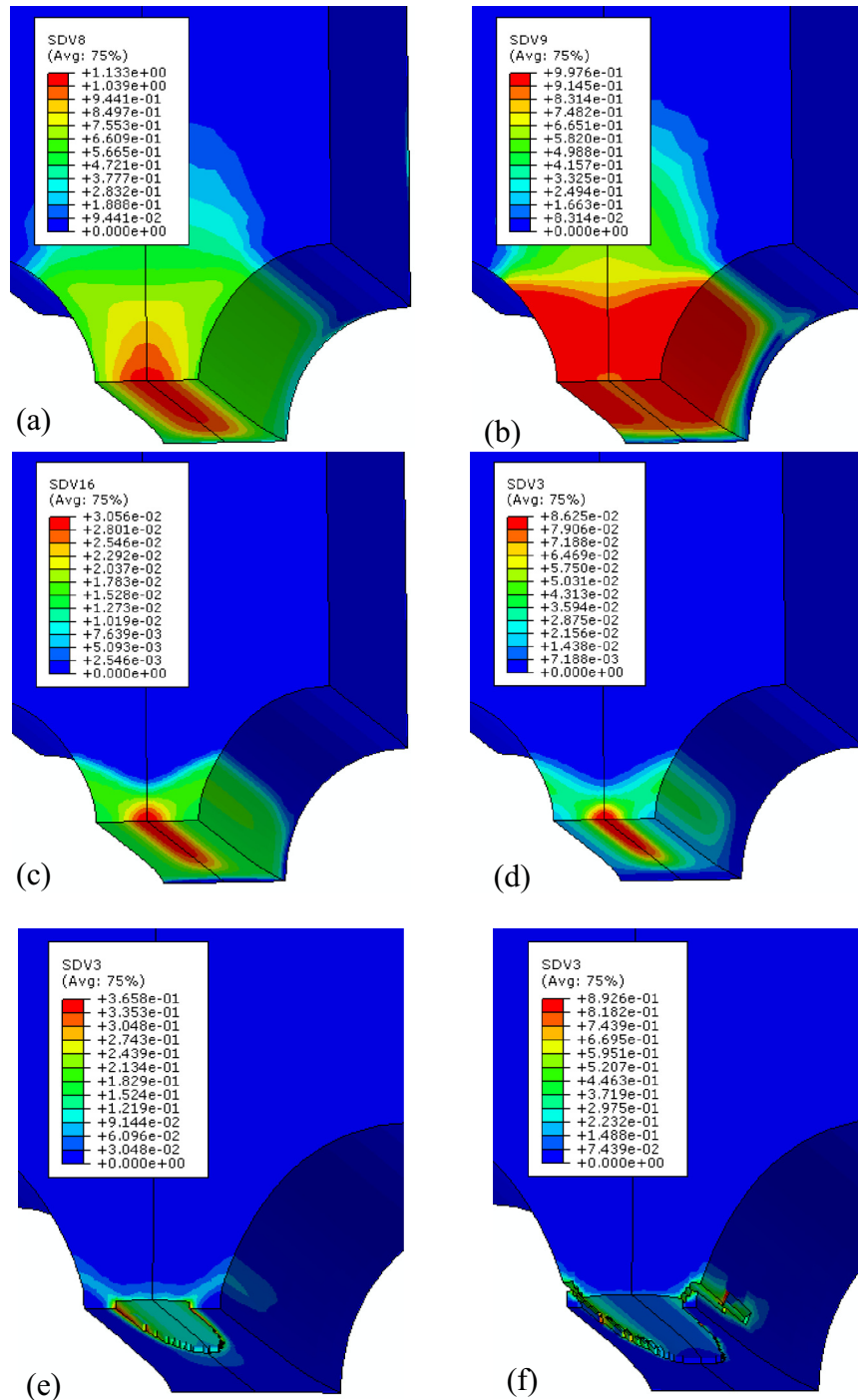
Fig. 19. Crack initiation and growth in the flat grooved plane strain tensile specimen: (a–d) contour plots of triaxiality, shear damage weight function, porosity and shear damage, before fracture initiation; (e) contour plot of shear damage after some amount of crack propagation; (f) final fracture.

4.2. Specimens

This study analyzes numerical models of smooth round tensile bars, notched round tensile bars, cylindrical compression specimens, the Lindholm-type torsion specimens subjected to pure torsion and combined torsion–compression, the flat notched tensile specimens, and the flat grooved plane strain tensile specimens. Fig. 9 shows sketches of these specimens. The experimental results for the testing of these specimens were reported in Zhai et al. (2014) and Zhang et al. (2012). The diameter of the gauge section of the smooth round tensile bar is 12.7 mm and the gauge length

is 50.8 mm. For the notched round bars, the diameter at the notch section is 7.62 mm, the notched radius is 2.54 mm, and the gauge length is 25.4 mm. The compression specimen has a diameter of 8.0 mm and length/diameter (*L*/*D*) ratio of 1.5. The Lindholm-type torsion specimen is a hollow cylinder having an inner diameter of 13.1 mm and outer diameter of 25.4 mm. The gauge section length and wall-thickness are 2.54 and 0.7366 mm respectively. Torsion–compression tests were performed with a central pin to prevent inward buckling. The flat notched tensile specimens have a thickness of 2.286 mm and the gauge section length is12.7 mm. The thickness of the flat grooved plane strain specimen at the groove
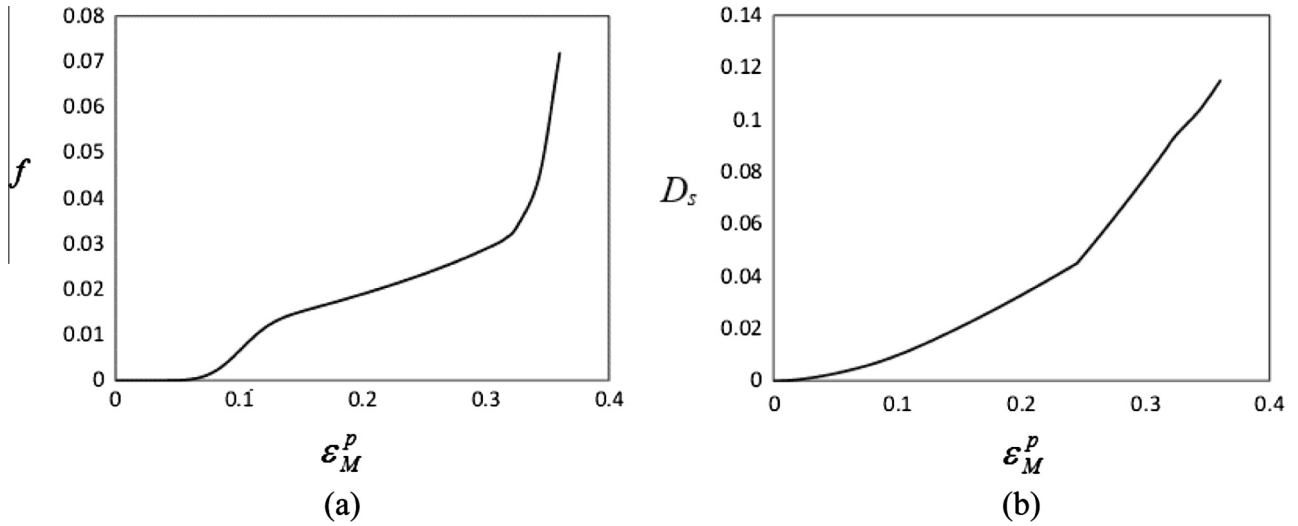
Fig. 20. Evolution of the void volume fraction and shear damage in the center element of the flat grooved plane strain tensile specimen.

is 2.032 mm, the radius of the groove is 2.032 mm, the plate thickness at the specimen shoulder is 6.096 mm, and the length of gauge section for this specimen is 12.7 mm.

4.3. Finite element procedure

ABAQUS/explicit is used to analyze all the specimens, where the material model is implemented via a user defined subroutine VUMAT. In the finite element analyses, 4-node axisymmetric elements with reduced integration (CAX4R) are used for round tensile specimens and the element size is 63.5×63.5 μm around the mid-plane where failure is expected to occur. Three-dimensional, 8-node brick elements with reduced integration (C3D8R) are used for all other specimens, where similar element size is adopted in critical regions. To improve model efficiency, symmetry conditions are applied whenever available. Fig. 10 shows typical finite element meshes of a round tensile specimen, a notched round bar tensile specimen, a compression specimen, a torsion specimen, a flat notched tensile specimen, and a flat grooved plane strain tensile specimen. For compression tests, the compression platen is modeled as a rigid surface, and frictional surface contact models the interaction between the platen and the specimen. Since the exact

friction coefficient is unknown and difficult to obtain, a value of 0.08 is used in the finite element analysis.

After the fully damaged material loses the ability to sustain hydrostatic tension load and shear load, it still can withstand pressure load. Therefore, special treatment is required after the complete failure of material under compressive stress states. Completely damaged material retains its bulk modulus for compressive hydrostatic loads. This corresponds to a fluid-like behavior. When the failed element under undergoes extremely large deformation, computational efficiency is reduced drastically, the element will be removed.

4.4. Results and discussion

4.4.1. Model calibration and verification

Model calibration follows a three-step strategy. For specimens where the onset of fracture is dominated by the void damage mechanism, the calibration of void related parameters can be conducted. The shear damage parameters can be calibrated using test data where fracture is dominated by shear damage. Finally the parameter k in the weight function of the shear damage evolution can be calibrated using experimental data obtained from a specimen with negative triaxiality and $g(\theta) \neq 1$.

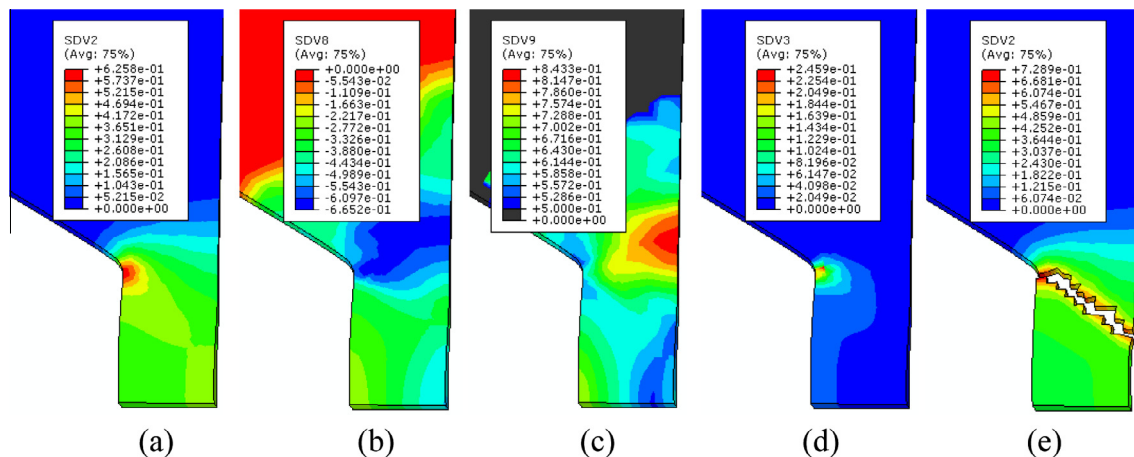

Fig. 21. Crack initiation and growth in the torsion–compression specimen: (a–d) contour plots of equivalent plastic strain, triaxiality, shear damage weight function and shear damage before fracture initiation; (e) final fracture.

Table 3 lists all calibrated material constants. The values of q_1 and q_2 are the suggested by Tvergaard (1981). Standard deviation of the void nucleation strain, S_n, is chosen to be a relatively small value to produce a rapid void nucleation process. Parameters f_n, f_c, and f_f, are calibrated from the smooth and notched round bar specimens. Effective failure strain under pure shear, ε_f^s, and the shear damage softening parameter n are calibrated from the pure torsion test. The value of parameter k is calibrated using the compression test data.

Fig. 11 provides comparisons of the load vs. displacement and torque vs. twist angle responses among numerical simulations and experimental data for specimens used in the calibrations. Since these specimens were used to fit material parameters, the extended GTN model with the calibrated model parameters predicts the plasticity responses and the onset of fracture very well for all the specimens.

To validate the calibrated model, the flat notched tensile specimen, the flat grooved plane strain tensile specimen and the torsion–compression specimen are analyzed. Fig. 12 provides comparisons of the load vs. displacement among numerical simulations and experimental data for the flat notched tensile specimen and the flat grooved plane strain tensile specimen respectively. The predictions of the load–displacement response and fracture onset agree with very well with experimental data.

Fig. 13 shows comparisons of the load vs. displacement and torque vs. twist angle responses among numerical simulations and experimental data for the torsion–compression specimen. This specimen is under negative triaxiality and the Lode angle is between pure shear and uniaxial compression. The comparison between model prediction and experimental data is reasonably well up until failure initiation. Experimental results show slowly softening after the peak load is reached which is not accurately captured by our model. There are several potential explanations. The weight function used to describe the stress state effect on shear damage may not be adequate. Alternatively, the newly created free surfaces contact and friction prevents rapid shear sliding. This behavior can provide some resistance to additional loading but is not included in the present model, which responses like a fluid (no shear resistance) after being fully damaged. These effects may be considered in further studies of fracture under negative triaxiality in the future.

4.4.2. Prediction of fracture initiation and propagation

To further examine the capability of the extended GTN model, prediction of fracture initiation, propagation and fracture surface appearance are discussed in this section. Figs. 14–20 provide the contour plots of several state variables during the loading history to show the volumetric and shear damage initiation, accumulation, and propagation process.

For the smooth round bar tensile specimen, as shown in Fig. 14, the crack initiates in the center of specimen where the triaxiality is high. The crack growth remains normal to the loading direction initially, is then followed by a slant fracture as it approaches to the specimen surface, and finally results in a cup–cone fracture surface. The notched round bar specimen does not show the cup–cone features, Fig. 15.

Fig. 16 shows fracture initiation occurs at the transition region in the pure torsion specimen due to strain concentration in this region (only a representative section is shown). The crack growth direction is normal to the direction of the applied torque.

For the compression specimen, Fig. 17 shows that fracture initiates at the top surface where the weight function has a higher value. The crack then propagates towards the specimen center, leading a slant fracture surface. Fig. 17(a) and (b) are obtained using a 1/8-symmetric finite element model while Fig. 17(c) shows the result of the full model where a coarser mesh is used to reduce the computational cost. In Fig. 17(d) is shown the picture of a failed specimen, confirming the features of the failure process and fracture surface predicted in Fig. 17(a)–(c).

Fig. 18 shows contour plots of flat notched tensile specimen, which is under a similar stress state as the notched round bar. Fracture starts in the center of the specimen, where it has the highest triaxiality, and propagates toward the specimen surface. The fracture surface is mostly flat, with a slight portion of slant fracture at the notch region where shear damage is caused by high plastic strain.

For the flat grooved plane strain specimen, both the stress triaxiality and the shear damage weight function have high values in a large region around the specimen center, Figs. 19(a) and (b). Contour plots of the void volume fraction and shear damage are given in Fig. 19(c) and (d). Fracture initiates at the center of the specimen and propagates to the sides of the specimen with a strong tunneling effect, as shown in Fig. 19(e). As the crack front approaches the specimen edge, shear damage is shown to be high in a slant plane, leading to the formation of a slant shear lip, Fig. 19(f).

Fig. 20 shows the evolution of the void volume fraction and shear damage in the center element of the flat grooved plane strain tensile specimen. Although the growth of the shear damage is not slow at the early stage, the void damage reaches the critical value first and void coalescence leads to the failure of this element.

Fig. 21 provides the contour plots of a representative section of torsion–compression specimen. Similar to the pure torsion test, crack initiation develops at the transition region. Crack growth follows a slant direction towards the center of the specimen.

5. Concluding remarks

In this paper, the GTN model is extended to account for the shear-induced damage by combining the damage mechanics concept with the void growth model. In particular, two damage parameters, the volumetric damage and the shear damage, are coupled into the yield function and flow potential. The evolution law for void volume fraction remains the same as in the original GTN model and a new shear damage evolution law is proposed. Separate critical conditions for the two types of damage are introduced. Complete material failure occurs once the total damage parameter reaches unity. The effectiveness of the new model is illustrated through a series of numerical tests comparing its performance with existing models. As an application, the model is employed to predict the ductile failure behavior of a beta-treated Zircaloy-4, where the plastic response of the undamaged matrix material exhibits tension–compression asymmetry, by coupling the proposed damage modeling framework with a recently developed J_2–J_3 plasticity model for the matrix material. The combined plasticity and ductile failure model is implemented in ABAQUS via a user defined subroutine. A model calibration scheme is presented and the material constants are determined based on experimental observations a semi-inverse method of matching the predicted load–displacement responses with experimental data for various specimens. The calibrated model predicts very well the load–displacement response, fracture initiation point, and propagation behavior in a variety of specimens, including specimens that exhibit zero or negative stress triaxiality.

Appendix A

The following summarizes the procedure of the single material point test which keeps the stress triaxiality and Lode parameter constant during the loading history.

Consider in the principal stress space and let $\bar{\sigma}$ be a proportionality factor. The mean stress can be expressed as

$$\sigma_m = \frac{1}{3}\sigma_{kk} = \beta\tilde{\sigma}. \tag{A1}$$

The three principal deviatoric stresses components can be expressed as

$$s_1 = \tilde{\sigma}, \quad s_2 = \alpha\tilde{\sigma}, \quad s_3 = (-1-\alpha)\tilde{\sigma}, \tag{A2}$$

where α and β are constants which can be related to the stress tri-axiality and Lode parameter and the three principal stresses can be expressed as

$$\boldsymbol{\sigma} = (1+\beta, \quad \alpha+\beta, \quad \beta-1-\alpha)^T\tilde{\sigma}. \tag{A3}$$

Therefore the von Mises equivalent stress can be expressed as $\sigma_e = \tilde{\sigma}\sqrt{3(1+\alpha+\alpha^2)}$ and the stress triaxiality and Lode angle can be related to constant α and β through

$$T^* = \frac{\beta}{\sqrt{3(1+\alpha+\alpha^2)}}$$
$$\theta = \tan^{-1}\left[\left(2\frac{2\alpha+1}{2+\alpha}-1\right)\frac{1}{\sqrt{3}}\right]. \tag{A4}$$

For any prescribed T^* and θ, parameters α and β can be solved from Eq. (A4). For θ varying from $-\pi/6$ to $\pi/6$, α varies from -0.5 to 1.

The values of α and β together with the value of $\tilde{\sigma}$ solved from Eq. (23b) determines the three principal stresses. Let $h_M = \partial\sigma_M/\partial\varepsilon_M^p$ be the tangent modulus of the matrix material, the following derivatives are needed to compute the hardening modulus, H, Eq. (22).

$$\frac{\partial f^*}{\partial f} = \begin{cases} 1 & \text{for} \quad f \leqslant f_c \\ \frac{1/q_1-f_c}{f_f-f_c} & \text{for} \quad f_c \leqslant f \leqslant f_f \end{cases},$$

$$\frac{\partial\Phi}{\partial\sigma_M} = -2\frac{\sigma_{eq}^2}{\sigma_M^3} - \frac{3q_1q_2f^*\sigma_m}{\sigma_M^2}\sinh\left(\frac{3q_2\sigma_m}{2\sigma_M}\right),$$

$$\frac{\partial\Phi}{\partial f^*} = 2q_1\cosh\left(\frac{3q_2\sigma_m}{2\sigma_M}\right) - 2q_1(q_1f^*+D_s),$$

$$\frac{\partial\Phi}{\partial D_s} = 2 - 2(q_1f^*+D_s), \tag{A5}$$

$$\frac{\partial\varepsilon_M^p}{\partial\lambda} = \frac{\sigma_{ij}n_{ij}}{(1-D/q_1)\sigma_M}, \frac{\partial f}{\partial\lambda} = (1-f)n_{kk} + A_n\frac{\partial\varepsilon_M^p}{\partial\lambda},$$

$$\frac{\partial D_s}{\partial\lambda} = \psi(\theta,T)\frac{nD_s^{\frac{n-1}{n}}}{\varepsilon_f^s}\frac{\partial\varepsilon_M^p}{\partial\lambda}.$$

References

Anderson, P.M., Fleck, N.A., Johnson, K.L., 1990. Localization of plastic deformation in shear due to microcracks. J. Mech. Phys. Solids 38, 681–699.

Benzerga, A.A., Leblond, J.-B., 2010. Ductile fracture by void growth to coalescence. Adv. Appl. Mech. 44, 169–305.

Chaboche, J., 1988. Continuum damage mechanics: Part II—damage growth, crack initiation, and crack growth. J. Appl. Mech. 55, 65–72.

Chu, C., Needleman, A., 1980. Void nucleation effects in biaxially stretched sheets. J. Eng. Mater. Technol. (Trans. ASME) 102, 249–256.

Cockeram, B., Chan, K., 2009. In situ studies and modeling the fracture of Zircaloy-4. J. Nucl. Mater. 393, 387–408.

Cockeram, B., Chan, K., 2013. In-situ studies and modeling of the deformation and fracture mechanism for wrought Zircaloy-4 and Zircaloy-2 as a function of stress-state. J. Nucl. Mater. 434, 97–123.

Gao, X., Faleskog, J., Shih, C.F., Dodds Jr., R.H., 1998. Ductile tearing in part-through cracks: experiments and cell-model predictions. Eng. Fract. Mech. 59, 761–777.

Gao, X., Shih, C.F., 1998. A parametric study of mixed-mode I/III ductile fracture in tough materials under small scale yielding. Eng. Fract. Mech. 60, 407–420.

Gao, X., Zhang, G., Roe, C., 2010. A study on the effect of the stress state on ductile fracture. Int. J. Damage Mech. 19, 75–94.

Gao, X., Zhang, T., Zhou, J., Graham, S.M., Hayden, M., Roe, C., 2011. On stress-state dependent plasticity modeling: significance of the hydrostatic stress, the third invariant of stress deviator and the non-associated flow rule. Int. J. Plast. 27, 217–231.

Gologanu, M., Leblond, J.-B., Devaux, J., 1993. Approximate models for ductile metals containing non-spherical voids—case of axisymmetric prolate ellipsoidal cavities. J. Mech. Phys. Solids 41, 1723–1754.

Gologanu, M., Leblond, J.-B., Devaux, J., 1994. Approximate models for ductile metals containing nonspherical voids–case of axisymmetric oblate ellipsoidal cavities. J. Eng. Mater. Technol. (Trans. ASME) 116, 290–297 (USA).

Gurson, A., 1977. Continuum theory of ductile rupture by void nucleation and growth: Part I—yield criteria and flow rules for porous ductile media. J. Eng. Mater. Technol. 99, 2.

Koplik, J., Needleman, A., 1988. Void growth and coalescence in porous plastic solids. Int. J. Solids Struct. 24, 835–853.

Lemaitre, J., 1985. A continuous damage mechanics model for ductile fracture. J. Eng. Mater. Technol. 107, 83–89.

Lemaitre, J., Lippmann, H., 1996. A Course on Damage Mechanics. Springer, Berlin.

Malcher, L., Andrade Pires, F., César de Sá, J., 2012. An assessment of isotropic constitutive models for ductile fracture under high and low stress triaxiality. Int. J. Plast. 30, 81–115.

McClintock, F.A., 1968. A criterion for ductile fracture by the growth of holes. J. Appl. Mech. 35, 363.

McClintock, F.A., Kaplan, S.M., Berg, C.A., 1966. Ductile fracture by hole growth in shear bands. Int. J. Fract. Mech. 2, 614–627.

Nahshon, K., Hutchinson, J., 2008. Modification of the Gurson model for shear failure. Eur. J. Mech. A/Solids 27, 1–17.

Nielsen, K.L., Tvergaard, V., 2009. Effect of a shear modified Gurson model on damage development in a FSW tensile specimen. Int. J. Solids Struct. 46, 587–601.

Nielsen, K.L., Tvergaard, V., 2010. Ductile shear failure or plug failure of spot welds modelled by modified Gurson model. Eng. Fract. Mech. 77, 1031–1047.

Rice, J.R., Tracey, D.M., 1969. On the ductile enlargement of voids in triaxial stress fields∗. J. Mech. Phys. Solids 17, 201–217.

Rousselier, G., 1987. Ductile fracture models and their potential in local approach of fracture. Nucl. Eng. Des. 105, 97–111.

Tvergaard, V., 1981. Influence of voids on shear band instabilities under plane strain conditions. Int. J. Fract. 17, 389–407.

Tvergaard, V., 1982. Influence of void nucleation on ductile shear fracture at a free surface. J. Mech. Phys. Solids 30, 399–425.

Tvergaard, V., Needleman, A., 1984. Analysis of the cup–cone fracture in a round tensile bar. Acta Metall. 32, 157–169.

Tvergaard, V., 2008. Shear deformation of voids with contact modelled by internal pressure. Int. J. Mech. Sci. 50, 1459–1465.

Tvergaard, V., 2009. Behaviour of voids in a shear field. Int. J. Fract. 158, 41–49.

Xia, L., Shih, C.F., Hutchinson, J.W., 1995. A computational approach to ductile crack growth under large scale yielding conditions. J. Mech. Phys. Solids 43, 389–413.

Xue, L., 2007. Damage accumulation and fracture initiation in uncracked ductile solids subject to triaxial loading. Int. J. Solids Struct. 44, 5163–5181.

Xue, L., 2008. Constitutive modeling of void shearing effect in ductile fracture of porous materials. Eng. Fract. Mech. 75, 3343–3366.

Zhai, J., Gao, X., Sobotka, J.C., Webler, B.A., Cockeram, B.V., 2014. Modeling the tension–compression asymmetry yield behavior of a β-treated Zircaloy-4. J. Nucl. Mater. 451, 292–299.

Zhang, T., Gao, X., Webler, B.A., Cockeram, B.V., Hayden, M., Graham, S.M., 2012. Application of the plasticity models that involve three stress invariants. Int. J. Appl. Mech. 4 (2), 1–24. http://dx.doi.org/10.1142/S1758825112500214.

Zhou, J., Gao, X., Hayden, M., Joyce, J.A., 2012. Modeling the ductile fracture behavior of an aluminum alloy 5083-H116 including the residual stress effect. Eng. Fract. Mech. 85, 103–116.